*J. Fluid Mech.* (2020), *vol.* 898, A17. © The Author(s), 2020.
Published by Cambridge University Press
doi:10.1017/jfm.2020.412





# Analysis of wall-pressure fluctuation sources from direct numerical simulation of turbulent channel flow

**Sreevatsa Anantharamu**[1] **and Krishnan Mahesh**[1,†]

[1]Aerospace Engineering and Mechanics, University of Minnesota – Twin Cities, Minneapolis, MN 55455, USA

(Received 13 November 2019; revised 23 March 2020; accepted 20 May 2020)

The sources of wall-pressure fluctuations in turbulent channel flow are studied using a novel framework. The wall-pressure power spectral density (PSD) ($\phi_{pp}(\omega)$) is expressed as an integrated contribution from all wall-parallel plane pairs, $\phi_{pp}(\omega) = \int_{-\delta}^{+\delta}\int_{-\delta}^{+\delta} \varGamma(r, s, \omega)\,\mathrm{d}r\,\mathrm{d}s$, using the Green's function. Here, $\varGamma(r, s, \omega)$ is termed the net source cross-spectral density (CSD) between two wall-parallel planes, $y = r$ and $y = s$ and $\delta$ is the half-channel height. Direct numerical simulation data at friction Reynolds numbers of 180 and 400 are used to compute $\varGamma(r, s, \omega)$. Analysis of the net source CSD, $\varGamma(r, s, \omega)$ reveals that the location of dominant sources responsible for the premultiplied peak in the power spectra at $\omega^+ \approx 0.35$ (Hu *et al.*, *AIAA J.*, vol. 44, 2006, pp. 1541–1549) and the wavenumber spectra at $\lambda^+ \approx 200$ (Panton *et al.*, *Phys. Rev. Fluids*, vol. 2, 2017, 094604) are in the buffer layer at $y^+ \approx 16.5$ and 18.4 for $Re_\tau = 180$ and 400, respectively. The contribution from a wall-parallel plane (located at distance $y^+$ from the wall) to wall-pressure PSD is log-normal in $y^+$ for $\omega^+ > 0.35$. A dominant inner-overlap region interaction of the sources is observed at low frequencies. Further, the decorrelated features of the wall-pressure fluctuation sources are analysed using spectral proper orthogonal decomposition (POD). Instead of the commonly used $L^2$ inner product, we require the modes to be orthogonal in an inner product with a symmetric positive definite kernel. Spectral POD supports the case that the net source is composed of two components – active and inactive. The dominant spectral POD mode that comprises the active part contributes to the entire wall-pressure PSD. The suboptimal spectral POD modes that constitute the inactive portion do not contribute to the PSD. Further, the active and inactive parts of the net source are decorrelated because they stem from different modes. The structure represented by the dominant POD mode at the premultiplied wall-pressure PSD peak inclines in the downstream direction. At the low-frequency linear PSD peak, the dominant mode resembles a large scale vertical pattern. Such patterns have been observed previously in the instantaneous contours of rapid pressure fluctuations by Abe *et al.* (2005, *Fourth International Symposium on Turbulence and Shear Flow Phenomena*, Begel House Inc.).

**Key words:** turbulence simulation, turbulent boundary layers, boundary layer structure

† Email address for correspondence: kmahesh@umn.edu

## 1. Introduction

In a turbulent flow, wall-pressure fluctuations excite flexible structures. The fluctuations' spatio-temporal features determine their relation to the far-field sound radiation resulting from the structural excitation. Pressure fluctuations in an incompressible flow are governed by the Poisson equation,

$$-\frac{\partial^2 p}{\partial x_i \partial x_i} = 2\rho \frac{\partial U_i}{\partial x_j}\frac{\partial u_j'}{\partial x_i} + \rho \frac{\partial^2}{\partial x_i \partial x_j}\left(u_i'u_j' - \overline{u_i'u_j'}\right), \tag{1.1}$$

with appropriate boundary conditions. Here, $p$ is the fluctuating pressure, $\rho$ is the constant fluid density and $U_i$ and $u_i'$ are the mean and fluctuating components of the flow velocities, respectively. The linear and quadratic (in fluctuation) source terms in the above equations are called the rapid and slow terms, respectively (Pope 2001). The Poisson equation implies that the pressure fluctuation is a global quantity, meaning that the velocity at every point in the domain affects $p$ at every point. This makes it harder to use arguments that are based on local length and velocity scale (that work reasonably well for local mean and fluctuating velocities) to analyse pressure fluctuations.

Several experiments (Willmarth & Wooldridge 1962; Corcos 1964; Blake 1970; Farabee & Casarella 1991; Gravante *et al.* 1998; Tsuji *et al.* 2007; Klewicki, Priyadarshana & Metzger 2008) and numerical simulations (Kim 1989; Choi & Moin 1990; Kim & Hussain 1993; Chang III, Piomelli & Blake 1999; Abe, Matsuo & Kawamura 2005; Hu, Morfey & Sandham 2006; Jimenez & Hoyas 2008; Sillero, Jiménez & Moser 2013; Park & Moin 2016; Panton, Lee & Moser 2017) have studied the spatio-temporal features of wall-pressure fluctuation in turbulent boundary layer and channel flows at different Reynolds numbers. Reviews by Willmarth (1975), Bull (1996) and Blake (2017) summarize the features of wall-pressure fluctuations in wall-bounded flows.

Farabee & Casarella (1991) measured wall-pressure fluctuations in a boundary layer at friction Reynolds numbers $Re_\tau = u_\tau \delta/\nu$ ranging from 1000–2000, where $u_\tau = \sqrt{\tau_w/\rho}$ is the friction velocity, $\delta$ is the boundary layer thickness, $\nu$ is the kinematic viscosity of the fluid, $\tau_w$ is the wall-shear stress and $\rho$ is the density of the fluid. Non-dimensionalization of the power spectral density (PSD) based on $\rho$, $U_o$ and $\delta^*$, where $\delta^*$ is the displacement thickness of the boundary layer, yielded collapse of the low-frequency region ($\omega\delta/u_\tau < 5$). The mid-frequency ($5 < \omega\delta/u_\tau < 100$) region showed collapse with outer flow variables ($u_\tau$, $\delta$, $\tau_w$), but the high-frequency region ($\omega\delta/u_\tau > 0.3Re_\tau$) collapsed with inner flow variables ($u_\tau$, $\nu$, $\tau_w$). An overlap region ($100 < \omega\delta/u_\tau < 0.3Re_\tau$) showed collapse with both outer and inner flow variables. Based on the wall-normal location associated with the corresponding non-dimensional variable group, Farabee & Casarella (1991) hypothesized the dominant contribution to the low-, mid- and high-frequency regions of the wall-pressure PSD to be from the unsteady potential region (above the boundary layer), outer region and inner region of the boundary layer, respectively.

Chang III *et al.* (1999) analysed the contribution of individual source terms to wall-pressure fluctuation PSD using Green's function formulation for $Re_\tau = 180$ channel flow. The contributions from the viscous sublayer, buffer, logarithmic and the outer region to wall-pressure fluctuation wavenumber spectra were investigated by computing partial pressures from sources located in the corresponding regions. The buffer region contribution was seen to be the most dominant for both slow and rapid terms over most of the wavenumber range. The logarithmic region was seen to contribute to the low wavenumbers through the rapid term. The viscous region was observed to contribute only to the high wavenumbers through both rapid and slow terms.

Panton *et al.* (2017) investigated wall-pressure fluctuations using direct numerical simulation (DNS) datasets of turbulent channel flow at $Re_\tau$ ranging from 180–5200. The premultiplied wall-pressure streamwise wavenumber spectra showed a peak around $\lambda_1^+ \approx 200$–300. Here, $\lambda_1^+$ is the non-dimensional streamwise wavelength based on inner units. Because the peak wavenumber scaled with inner units, Panton *et al.* (2017) believed the location of the corresponding velocity sources to be in the inner region of the channel. Further, with increasing Reynolds number, the low wavenumber contribution was observed to increase in magnitude and separate from the high-wavenumber contribution. Since the dominant low wavenumbers did not scale with inner units, the corresponding velocity sources were believed to be in the outer region of the channel. Hence, the outer region contribution to wall-pressure becomes important at very high Reynolds numbers.

We investigate the decorrelated features of wall-pressure fluctuation sources in the turbulent channel using spectral proper orthogonal decomposition (spectral POD). Spectral POD was originally introduced by Lumley (2007) and recently analysed by Towne, Schmidt & Colonius (2018) for its relation to dynamic mode decomposition and resolvent analysis. It involves the eigendecomposition of the cross-spectral density of the quantity of interest. The technique has been used previously (Schmidt *et al.* 2018) as a post-processing tool to infer wavepackets in axisymmetric jets. We use this technique to obtain the decorrelated contribution from each wall-parallel plane to wall-pressure fluctuation PSD. To our knowledge, this is the first work that uses spectral POD to analyse wall-pressure fluctuation sources.

Unlike the methodology of Chang III *et al.* (1999), the proposed method takes into account the wall-normal cross-correlation of the source terms and accounts for the phase relationships between different wall-parallel planes. The contribution of cross-correlation between sources in any two wall-parallel planes to wall-pressure PSD is quantified as a function of frequency. Also, the collapse of the frequency and wavenumber spectrum based on inner and outer flow variables as carried out in Farabee & Casarella (1991) and Panton *et al.* (2017) do not yield such information on the wall-normal distribution, insight into which can be obtained from the proposed analysis. A 'net source distribution function' (also termed as 'net source' for brevity) is defined which yields the integrated effect of all sources in a particular wall-parallel plane. The cross-spectral density (CSD) of the net source function is computed from the generated DNS database. The net source CSD when doubly integrated in the wall-normal direction yields the wall-pressure PSD and, when singly integrated yields the CSD between wall-pressure fluctuation and the net source. In addition to the spectral features, spectral POD is used to identify the decorrelated contribution from each wall-parallel plane. We present a parallel implementation of the analysis framework that is streaming, thus enabling processing of large datasets.

The paper is organized as follows. We discuss the DNS simulation details in § 2. The theory and implementation of the proposed analysis framework to investigate wall-pressure sources is discussed in §§ 3.1 and 3.2, respectively. Finally, in § 4, we discuss the spectral features of the net source function, the spectral POD results and their relevance to wall-pressure fluctuation PSD using DNS data at $Re_\tau = 180$ and 400.

## 2. DNS simulation details

The incompressible Navier–Stokes equations are solved using the collocated finite volume method of Mahesh, Constantinescu & Moin (2004) in a frame of reference

| $Re_\tau$ | $N_x \times N_y \times N_z$ | $\Delta x^+$ | $\Delta z^+$ | $\Delta y_w^+$ | $\Delta y_c^+$ | $U_{bref}^+$ | $Tu_\tau/\delta$ |
|---|---|---|---|---|---|---|---|
| 180 | $720 \times 176 \times 330$ | 4.7 | 3.4 | 0.27 | 4.4 | 15.8 | 8 |
| 400 | $1388 \times 288 \times 660$ | 5.4 | 3.8 | 0.37 | 5.9 | 17.8 | 8 |

TABLE 1. Grid sizes, mesh spacing and velocity of the moving frame of reference used in the DNS simulation.

moving with the bulk velocity of the fluid as done by Bernardini *et al.* (2013). Better prediction of the convection velocities and high-wavenumber component of the streamwise velocity fluctuations was observed by Bernardini *et al.* (2013) in the moving frame of reference. We observed a slightly better prediction of the high-frequency component of the wall-pressure frequency spectra with the moving frame of reference formulation. The method is second-order accurate in space. We use the Crank–Nicolson time integration scheme to ensure second-order accuracy in time and to allow for larger time steps. The method uses a least-square cell-centred pressure gradient reconstruction to ensure discrete kinetic energy conservation in space. This ensures stability at large Reynolds number without adding numerical dissipation.

We define the subscripts $x$, $y$ and $z$ to be the streamwise, wall-normal and spanwise directions. The computational domain is a Cartesian box with side lengths $L_x = 6\pi\delta$, $L_y = 2\delta$ and $L_z = 2\pi\delta$. A long streamwise domain was chosen to include the large scale contribution within the domain. Also, the long domain eliminates periodicity effects otherwise seen in low-frequency streamwise wavenumber frequency spectra (not shown). The spurious high levels of the low-wavenumber region observed in the results of Choi & Moin (1990) at low frequencies is not present in the current simulation results (not shown). Table 1 shows the grid sizes $(N_x, N_y, N_z)$ for $Re_\tau = 180$ and 400. The mesh is uniform in the streamwise and spanwise directions, and a hyperbolic tangent spacing is used in the wall-normal direction with a stretching factor of 2.07 for both $Re_\tau$. The mesh spacing in viscous units ($\Delta x^+$, $\Delta z^+$, $\Delta y_w^+$, $\Delta y_c^+$) is given in table 1, where $\Delta y_w^+$, $\Delta y_c^+$ is the wall-normal mesh spacing at the wall and at the centreline respectively. A superscript of $+$ indicates non-dimensionalization with respect to inner layer variables $u_\tau$ and $\nu$ respectively. The resolution is sufficient enough to resolve the near-wall fine scale features. The velocity of the moving frame of reference ($U_{bref}^+$) is chosen to be 15.8 and 17.8 for $Re_\tau = 180$ and 400 respectively. These values are close to the actual bulk velocity in the stationary frame of reference. A non-dimensional body force ($f_x\delta/\rho u_\tau^2$) of 1 is applied in the streamwise direction throughout the domain. A slip velocity equal to the negative of the frame velocity is applied at the walls. Periodic boundary conditions are used in the streamwise and spanwise directions. A time step of $5 \times 10^{-4}\delta/u_\tau$ is used for both the simulations. The flow is initially transient and subsequently reaches a statistically stationary state when the discharge starts to oscillate around a mean value. The total simulation time for both $Re_\tau = 180$ and 400 cases is $8\delta/u_\tau$ after the initial transient period. We sample the data every time step to compute wall-pressure statistics.

## 3. Analysis framework

### 3.1. *Theory*

We first write the solution to (1.1) using the Green's function formulation. The streamwise and spanwise extents are taken to be infinite and the frame of reference is assumed to be stationary. We use a zero normal derivative of the pressure fluctuation as the boundary condition at the top and bottom walls. The Stokes component of pressure arising from the non-zero wall-normal derivative of wall-pressure fluctuation at the top and bottom wall has been shown to be negligible when compared to the rapid and slow terms for high Reynolds number flows (Hoyas & Jiménez 2006; Gerolymos, Sénéchal & Vallet 2013). The wall-normal coordinates of the top and bottom wall are $y=+\delta$ and $y=-\delta$ respectively. The Fourier transform is defined as

$$g(t)=\int_{-\infty}^{\infty}\hat{g}(\omega)\mathrm{e}^{\mathrm{i}\omega t}\,\mathrm{d}\omega;\quad \hat{g}(\omega)=\frac{1}{2\pi}\int_{-\infty}^{\infty}g(t)\mathrm{e}^{-\mathrm{i}\omega t}\,\mathrm{d}t, \tag{3.1$a$,$b$}$$

where $\hat{g}(\omega)$ is the Fourier transform of $g(t)$. The pressure fluctuation

$$\left.\begin{aligned} p(x,y,z,t)&=\iint_{-\infty}^{\infty}\hat{p}(k_1,y,k_3,t)\mathrm{e}^{\mathrm{i}(k_1x+k_3z)}\,\mathrm{d}k_1\,\mathrm{d}k_3,\\ \hat{p}(k_1,y,k_3,t)&=\int_{-\delta}^{+\delta}G(y,y',k_1,k_3)\hat{f}(k_1,y,k_3,t)\,\mathrm{d}y',\\ \hat{f}(k_1,y,k_3,t)&=\frac{1}{(2\pi)^2}\iint_{-\infty}^{\infty}f(x,y,z,t)\mathrm{e}^{-\mathrm{i}(k_1x+k_3z)}\,\mathrm{d}x\,\mathrm{d}z, \end{aligned}\right\} \tag{3.2}$$

where $f(x,y,z,t)$ is the right-hand side source term in the Poisson equation (equation (1.1)), $\hat{p}(k_1,y,k_3,t)$ and $\hat{f}(k_1,y,k_3,t)$ denote the Fourier transform in the spanwise and streamwise directions of $p(x,y,z,t)$ and $f(x,y,z,t)$ respectively, and the Fourier transform $\hat{p}(k_1,y,k_3,t)$ is defined similar to $\hat{f}(k_1,y,k_3,t)$ in the above equation. The Green's function $G(y,y',k_1,k_3)$ can be shown to be

$$\left.\begin{aligned} G(y,y',k_1,k_3)&=\begin{cases}\dfrac{\cosh(k(y'-\delta))\cosh(k(y+\delta))}{2k\sinh(k\delta)\cosh(k\delta)}, & y\leqslant y',\\[2ex] \dfrac{\cosh(k(y'+\delta))\cosh(k(y-\delta))}{2k\sinh(k\delta)\cosh(k\delta)}, & y>y',\end{cases}\\ k&=\sqrt{k_1^2+k_3^2}, \end{aligned}\right\} \tag{3.3}$$

for all combinations of $k_1, k_3$ except when both $k_1=0$ and $k_3=0$, for which we can obtain

$$G(y,y',k_1,k_3)=\begin{cases}\tfrac{1}{2}(y-y'), & y\leqslant y',\\ \tfrac{1}{2}(y'-y), & y>y'.\end{cases} \tag{3.4}$$

In order to ensure uniqueness of the Green's function when $k=0$, we have made use of the condition that the instantaneous average of the top and bottom wall-pressure fluctuation is zero. The above Green's function has been previously used by Kim (1989) to obtain wall-pressure fluctuations from the Kim, Moin & Moser (1987) simulation.

The wall-pressure fluctuation of a point $(x,z)$ on the bottom wall is

$$\begin{aligned} p(x,-\delta,z,t)&=\iint_{-\infty}^{\infty}p(k_1,-\delta,k_3,t)\mathrm{e}^{\mathrm{i}(k_1x+k_3z)}\,\mathrm{d}k_1\mathrm{d}k_3,\\ &=\iint_{-\infty}^{\infty}\int_{-\delta}^{+\delta}G(-\delta,y,k_1,k_3)f(k_1,y,k_3,t)\,\mathrm{d}y\mathrm{e}^{\mathrm{i}(k_1x+k_3z)}\,\mathrm{d}k_1\,\mathrm{d}k_3, \end{aligned}$$

$$= \int_{-\delta}^{+\delta} \iint_{-\infty}^{\infty} G(-\delta, y, k_1, k_3) f(k_1, y, k_3, t) \mathrm{e}^{\mathrm{i}(k_1 x + k_3 z)} \, \mathrm{d}k_1 \, \mathrm{d}k_3 \, \mathrm{d}y,$$
$$= \int_{-\delta}^{+\delta} f_G(x, y, z, t) \, \mathrm{d}y, \tag{3.5}$$

where $f_G(x, y, z, t)$ is termed the 'net source' because it includes contribution from all sources in a wall-parallel plane and the Green's function. It includes the contribution from all streamwise and spanwise wavenumbers. The Green's function essentially assigns a weight to each wavenumber $(k_1, k_3)$ component of the source in the wall-parallel plane. Note that the function $f_G(x, y, z, t)$ is homogeneous in the streamwise and spanwise directions.

In order to characterize the features of the net source function $f_G(x, y, z, t)$, the net source CSD $\Gamma(r, s, \omega)$ is defined as

$$\Gamma(r, s, \omega) = \frac{1}{2\pi} \int_{-\infty}^{\infty} \langle f_G^*(x, r, z, t) f_G(x, s, z, t+\tau) \rangle \mathrm{e}^{-\mathrm{i}\omega\tau} \, \mathrm{d}\tau. \tag{3.6}$$

It can be related to the five-dimensional CSD $\varphi_{ff}(r, s, k_1, k_3, \omega)$ of the pressure Poisson source terms as

$$\Gamma(r, s, \omega) = \iint_{-\infty}^{+\infty} G^*(0, r, \mathrm{k}_1, \mathrm{k}_3) G(0, s, \mathrm{k}_1, \mathrm{k}_3) \varphi_{ff}(r, s, k_1, k_3, \omega) \, \mathrm{d}k_1 \, \mathrm{d}k_3, \tag{3.7}$$

where

$$\varphi_{ff}(r, s, k_1, k_3, \omega) = \frac{1}{(2\pi)^3} \iiint_{-\infty}^{+\infty} \langle f^*(x, r, z, t) f(x+\xi_1, s, z+\xi_3, t+\tau) \rangle \times \mathrm{e}^{-\mathrm{i}(k_1\xi_1 + k_3\xi_3 + \omega\tau)} \, \mathrm{d}\xi_1 \, \mathrm{d}\xi_3 \, \mathrm{d}\tau. \tag{3.8}$$

The PSD of the spatially homogeneous wall-pressure fluctuation $\phi_{pp}(\omega)$ is related to the net source CSD.

$$\phi_{pp}(\omega) = \int_{-\delta}^{+\delta} \int_{-\delta}^{+\delta} \Gamma(r, s, \omega) \, \mathrm{d}r \, \mathrm{d}s. \tag{3.9}$$

In order to analyse the contribution from a particular wall-parallel plane at $y = r$, we include its cross-correlation with every other wall-normal location $y' = s$ by integrating $\Gamma(r, s, \omega)$ along $s$.

$$\Psi(r, \omega) = \int_{-\delta}^{+\delta} \Gamma(r, s, \omega) \, \mathrm{d}s. \tag{3.10}$$

The resulting function $\Psi(r, \omega)$ can be shown to be the CSD of the wall-pressure fluctuation and the net source at $r$, i.e.

$$\Psi(r, \omega) = \frac{1}{2\pi} \int_{-\infty}^{\infty} \langle f_G^*(x, r, z, t) p(x, -1, z, t+\tau) \rangle \mathrm{e}^{-\mathrm{i}\omega\tau} \, \mathrm{d}\tau. \tag{3.11}$$

We will call $\Psi(r, \omega)$ the wall-pressure fluctuation – net source CSD. The wall-pressure PSD can be expressed in terms of $\Psi(r, \omega)$.

$$\phi_{pp}(\omega) = \int_{-\delta}^{+\delta} \Psi(r, \omega) \, \mathrm{d}r. \tag{3.12}$$

Next, we identify decorrelated features in the dataset that contribute the most to the wall-pressure PSD using $\varGamma(r, s, \omega)$. To accomplish this, we use the Poisson inner product defined in (3.16) to enforce the orthonormality of the eigenfunctions instead of the commonly used $L^2$ inner product. We decompose $\varGamma(r, s, \omega)$ as

$$\varGamma(r, s, \omega) = \sum_{i=1}^{\infty} \lambda_i(\omega)\varPhi_i(r, \omega)\varPhi_i^*(s, \omega), \tag{3.13}$$

where $\{\lambda_i(\omega), \varPhi_i(r, \omega)\}_{i=1}^{\infty}$ are the spectral POD eigenvalue and mode pairs. The mode $\varPhi_i(r, \omega)$ relates to the eigenfunction $\bar{\varPhi}_i(r, \omega)$ of $\varGamma(r, s, \omega)$ through the relation

$$\varPhi_i(r, \omega) = \left(-(1-\beta)\frac{\partial^2}{\partial y^2} + \beta\right)\bar{\varPhi}_i(r, \omega), \tag{3.14}$$

where $\beta$ is a real number satisfying $0 < \beta \leqslant 1$ and the eigenfunctions are assumed to satisfy zero Neumann boundary conditions $\bar{\varPhi}_i(r, \omega)$ at $r = -\delta$ and $r = +\delta$. The eigenvalue problem for $\bar{\varPhi}_i(r, \omega)$ and $\lambda_i(\omega)$ is

$$\int_{-\delta}^{+\delta} \varGamma(r, s, \omega)\bar{\varPhi}_i(s, \omega)\,\mathrm{d}s = \lambda_i(\omega)\left(-(1-\beta)\frac{\partial^2}{\partial y^2} + \beta\right)\bar{\varPhi}_i(r, \omega). \tag{3.15}$$

The spectral POD eigenvalues are arranged in decreasing order. The eigenfunctions $\bar{\varPhi}_i(r, \omega)$ satisfy the orthonormality condition

$$\left.\begin{aligned} &= \int_{-\delta}^{+\delta} \bar{\varPhi}_i^*(r, \omega)\left(-(1-\beta)\frac{\partial^2}{\partial y^2} + \beta\right)\bar{\varPhi}_j(r, \omega)\,\mathrm{d}r \\ &= \delta_{ij}, \end{aligned}\right\} \tag{3.16}$$

where $\delta_{ij}$ is the Kronecker delta. We will call the inner product above 'the Poisson inner product' because the kernel $(-(1-\beta)(\partial^2/\partial y^2) + \beta)$ can be related to the Poisson equation. If we choose $\beta = 1$, then the Poisson inner product is the standard $L^2$ inner product.

The contribution of each spectral POD mode to wall-pressure PSD can be obtained by integrating equation (3.13) in $r$ and $s$,

$$\phi_{pp}(\omega) = \sum_{i=1}^{\infty} \gamma_i(\omega); \quad \gamma_i(\omega) = \lambda_i(\omega)\left|\int_{-\delta}^{+\delta} \varPhi_i(r, \omega)\,\mathrm{d}r\right|^2; \quad i = 1, \ldots, \infty. \tag{3.17a,b}$$

In the above equation, the wall-pressure PSD is expressed as sum of positive contributions $\{\gamma_i(\omega)\}_{i=1}^{\infty}$ from each spectral POD mode. We will use the quantities $\{\gamma_i(\omega)\}_{i=1}^{\infty}$ to identify the spectral POD modes that are the dominant contributors to wall-pressure PSD.

The spectral POD modes and eigenvalues depend on the parameter $\beta$. For a chosen value of $\beta$, we will have the corresponding set of spectral POD modes $\{\varPhi_i(y, \omega)\}_{i=1}^{\infty}$ and eigenvalues $\{\lambda_i(\omega)\}_{i=1}^{\infty}$. However, irrespective of the chosen $\beta$, the component of the net source Fourier transform $(\hat{f}_G(x, y, z, \omega))$ along the spectral POD modes will be decorrelated, i.e.

$$\left.\begin{aligned} f_G(x, y, z, t) &= \int_{-\infty}^{+\infty} \hat{f}_G(x, y, z, \omega)\mathrm{e}^{\mathrm{i}\omega t}\,\mathrm{d}\omega, \\ \hat{f}_G(x, y, z, \omega) &= \sum_{j=1}^{\infty} \alpha_j(x, z, \omega)\varPhi_j^*(y, \omega), \\ \langle \alpha_i(x, z, \omega)\alpha_j^*(x, z, \omega_o)\rangle &= \lambda_i(\omega)\delta_{ij}\delta(\omega - \omega_o), \end{aligned}\right\} \tag{3.18}$$

where $\{\alpha_j(x, z, \omega)\}_{j=1}^{\infty}$ are the coefficients, $\langle\cdot\rangle$ denotes ensemble average and $\delta$ is the Dirac delta function.

On the other hand, choosing the $L^2$ inner product ($\beta = 1$) to enforce the orthonormality of the modes will also optimally decompose the wall-normal integral of the PSD $\Gamma(r, r, \omega)$. Substituting $s = r$ in (3.13) and integrating in $r$, we obtain

$$\left.\begin{aligned} \Gamma(r, r, \omega) &= \sum_{j=1}^{\infty} \lambda_j(\omega)|\Phi_i(r, \omega)|^2, \\ \int_{-\delta}^{+\delta} \Gamma(r, r, \omega)\,\mathrm{d}r &= \sum_{j=1}^{\infty} \lambda_j(\omega). \end{aligned}\right\} \tag{3.19}$$

However, the dominant spectral POD modes obtained with the $L^2$ inner product do not necessarily isolate the main contribution to the wall-pressure PSD. i.e. the value of $\gamma_i(\omega)$. That is, the wall-pressure PSD can be distributed over a large number of modes that each individually contribute a small fraction. This makes it difficult to identify the few dominant decorrelated source patterns. Further, the single dominant wall-pressure mode (mode with largest $\gamma_i(\omega)$) does not necessarily contain any useful information about the source because it contributes only a small fraction to the wall-pressure PSD. This was observed at low frequencies (see figure 16).

Our goal is to identify useful decorrelated features of the wall-pressure source, not to optimally decompose the integrated net source PSD (as done by the $L^2$ inner product). Therefore, we use the parameter $\beta$ to our advantage and select a suitable value for $\beta$.

For $0 < \beta < 1$, it can be shown that the Poisson inner product optimally decomposes $\int\int_{-\delta}^{+\delta} G(s, r, \beta/(1-\beta), 0)/(1-\beta)\Gamma(r, s, \omega)\,\mathrm{d}r\,\mathrm{d}s$ into the sum of spectral POD eigenvalues,

$$\iint_{-\delta}^{+\delta} \frac{G\left(s, r, \dfrac{\beta}{1-\beta}, 0\right)}{1-\beta} \Gamma(r, s, \omega)\,\mathrm{d}r\,\mathrm{d}s = \sum_{j=1}^{\infty} \lambda_j(\omega), \tag{3.20}$$

where the Green's function $G$ is given in (3.3). We can observe that as $\beta$ approaches 0, the Green's function $G(r, s, \beta/(1-\beta), 0)$ becomes flatter and approaches a function that is constant in $r$ and $s$. Thus, the left-hand side in the above equation approaches the wall-pressure PSD $\phi_{pp}(\omega) = \iint_{-1}^{+1} \Gamma(r, s, \omega)\,\mathrm{d}r\,\mathrm{d}s$ (up to a scaling). As we decrease $\beta$, we can therefore expect the dominant spectral POD modes to be the dominant contributors to wall-pressure PSD. Therefore, the Poisson inner product in (3.16) identifies the few dominant features of wall-pressure sources that are decorrelated.

The Poisson inner product defined in (3.16) does not fall into the category presented by Towne *et al.* (2018). They required the eigenfunctions to be orthonormal in a weighted $L^2$ inner product. Here, we use the Poisson inner product (3.16) that has a symmetric positive definite kernel.

The set of spectral POD modes obtained with any $\beta$ is complete. Therefore, we can relate the POD modes obtained with two different values of $\beta$ to each other through a linear transformation. That is, if $\{\hat{\Phi}_i(y, \omega)\}_{i=1}^{\infty}$ and $\{\tilde{\Phi}_i(y, \omega)\}_{i=1}^{\infty}$ are the two sets of spectral POD modes obtained with two different values of $\beta$, then

$$\hat{\Phi}_i(y, \omega) = \sum_j C_{ij}^*(\omega)\tilde{\Phi}_j(y, \omega), \tag{3.21}$$

where the matrix $C(\omega) = [C_{ij}(\omega)]$ is the linear transformation. Further, we show in appendix B that the linear transformation $C(\omega)$ is indeed orthogonal with an appropriate row scaling, i.e.

$$(\hat{\Lambda}^{1/2}(\omega)C(\omega))^H \hat{\Lambda}^{1/2}(\omega)C(\omega) = \tilde{\Lambda}(\omega), \tag{3.22}$$

where $\hat{\Lambda}(\omega)$ and $\tilde{\Lambda}(\omega)$ are the diagonal matrices of eigenvalues of the set of modes $\{\hat{\Phi}_i(y, \omega)\}_{i=1}^{\infty}$ and $\{\tilde{\Phi}_i(y, \omega)\}_{i=1}^{\infty}$, respectively.

We can show that

$$\left| \int_{-\delta}^{+\delta} \Phi_i(y, \omega)\, \mathrm{d}y \right| = \int_{-\delta}^{+\delta} |\Phi_i(y, \omega)| \cos(\angle \Phi_i(y, \omega) - \angle \Phi_i^n(\omega))\, \mathrm{d}y, \tag{3.23}$$

where $\angle \Phi_i^n(\omega) = \angle(\int_{-\delta}^{+\delta} \Phi_i(y, \omega)\, \mathrm{d}y)$ and $\angle$ denotes the phase of the complex number that follows it. Using (3.23) in (3.17), we obtain

$$\gamma_i(\omega) = \lambda_i(\omega) \left( \int_{-\delta}^{+\delta} |\Phi_i(r, \omega)| \cos(\angle \Phi_i(r, \omega) - \angle \Phi_i^n(\omega))\, \mathrm{d}r \right)^2; \quad i = 1, \ldots, \infty. \tag{3.24}$$

From the above equation, we can observe that the eigenvalue, magnitude and phase of the spectral POD mode, all play a role in determining its contribution to wall-pressure PSD. Sources contained in wall-normal regions where the phase is in the range $|\angle \Phi_i(y, \omega) - \angle \Phi_i^n(\omega)| < \pi/2$ undergo destructive interference with the sources contained in the region where $\pi/2 < |\angle \Phi_i(y, \omega) - \angle \Phi_i^n(\omega)| < \pi$. Therefore, the interference of the sources from different wall-normal regions represented by a spectral POD mode plays a role in determining the net contribution to wall-pressure PSD from the mode.

### 3.2. *Implementation*

The five-dimensional CSD $\varphi_{ff}(r, s, k_1, k_3, \omega)$ defined in (3.8) contains all pertinent information on velocity field sources from cross-correlation of two wall-normal locations. However, computing the function is extremely memory intensive. For the $Re_\tau = 400$ case, assuming 2000 frequencies, we would need $\approx$1220 TB to store $\varphi_{ff}$. We use a streaming parallel implementation procedure to compute the net source CSD $\Gamma(r, s, \omega)$ that makes the computation feasible.

The source term in (1.1) is computed and stored from the DNS. The stored data are divided into multiple chunks to compute the ensemble average in (3.8). For a given chunk, the source terms are first converted to stationary frame of reference and then Fourier transformed in $x$, $z$ and $t$. The Fourier transforms are then used to update the net source CSD. Details of the parallel implementation are provided in appendix A.

A total of 16 000 time steps are used to obtain the net source CSD $\Gamma(r, s, \omega)$ for both $Re_\tau$. We sample the data every time step. The number of time steps in each chunk is 2000 and 50 % overlap is used in time to increase statistical convergence. The frequency resolution of the analysis is $\Delta\omega\delta/u_\tau = 2\pi$.

## 4. Results and discussion

First, we discuss the spectral features of the wall-pressure fluctuations obtained from the finite volume solver. Then, the wall-pressure net source cross-spectral density (wall-pressure fluctuation – net source CSD) and the dominant decorrelated net source patterns obtained using spectral POD are discussed. For validation of the current DNS, we refer the reader to appendix C.

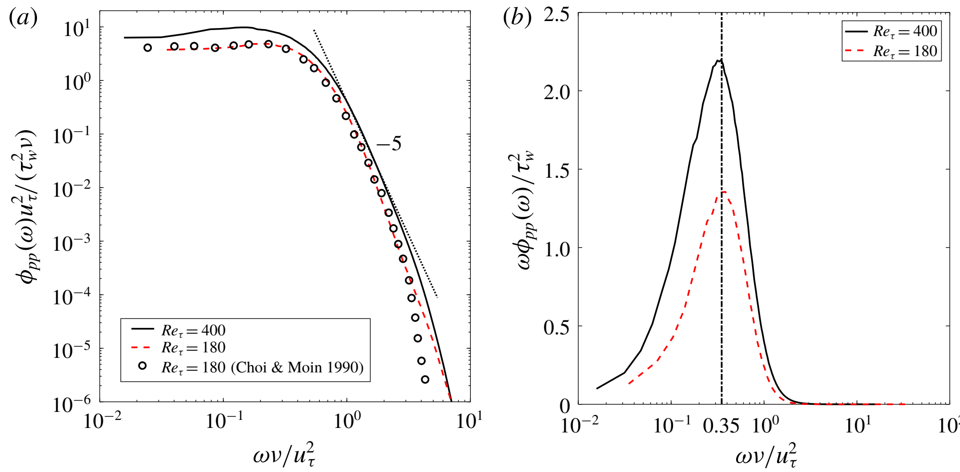


FIGURE 1. Wall-pressure fluctuation power spectra in (*a*) inner units and (*b*) premultiplied form with inner units on *x*-axis.

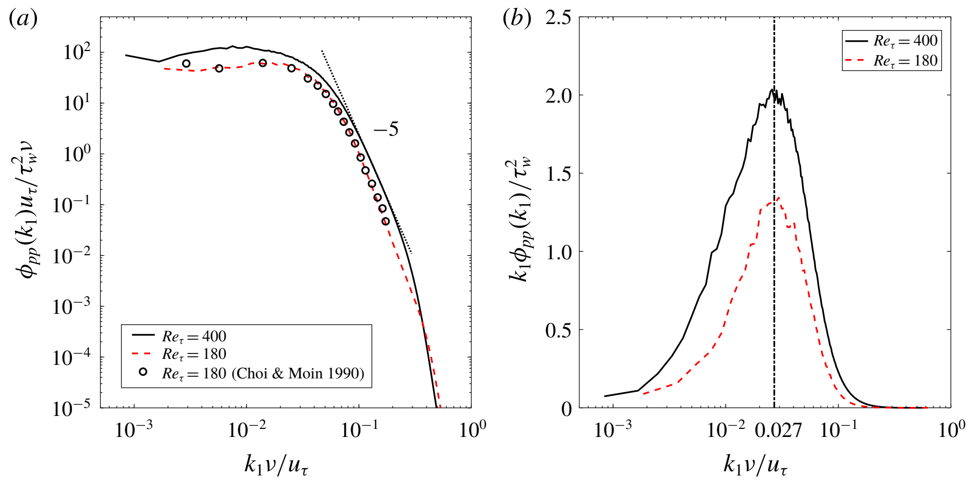


FIGURE 2. Wall-pressure fluctuation streamwise wavenumber spectra in (*a*) inner units and (*b*) premultiplied form with inner units on *x*-axis.

### 4.1. *DNS wall-pressure fluctuations*

The one-sided PSD of the obtained $Re_\tau = 180$ and 400 wall-pressure fluctuations scaled with inner variables is shown in figure 1(*a*). The streamwise wavenumber spectra of the fluctuations at the two $Re_\tau$ are shown in figure 2(*a*). Both the PSD and wavenumber spectra at $Re_\tau = 180$ agree well with the results of Choi & Moin (1990). The high-frequency region with $\omega^+ = \omega\nu/u_\tau^2 > 1$, shows a small region of −5 decay for the higher Reynolds number ($Re_\tau = 400$). The high-wavenumber region of the wavenumber spectra plotted in figure 2(*a*) also shows a small region of −5 decay in the region $k_1^+ = k_1\nu/u_\tau > 0.1$, for the $Re_\tau = 400$ case. The premultiplied power spectra plotted in figure 1(*b*) for both $Re_\tau$ show a peak at $\omega_p^+ = 0.35$. This peak at the same frequency has been previously observed by Hu *et al.* (2006) for $Re_\tau$ up to 1440.

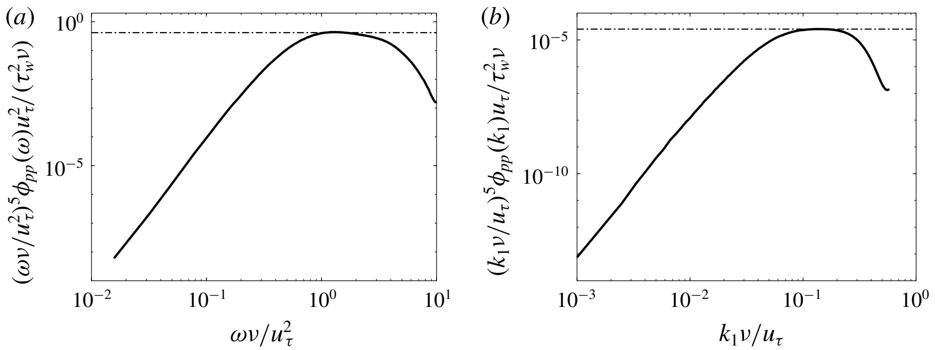


FIGURE 3. Diagnostic function to verify region of −5 slope in the $Re_\tau = 400$ (*a*) power and (*b*) streamwise wavenumber spectrum. The dashed-dotted horizontal lines in (*a*) and (*b*) indicate constant values of 0.42 and $2.53 \times 10^{-5}$, respectively.

Similar to the power spectra, the premultiplied streamwise wavenumber spectra in figure 2(*b*) also show a peak at $k_1^+ = k_1\nu/u_\tau$ at $k_p^+ = 0.027$. This peak has also been previously observed by Panton *et al.* (2017) for $Re_\tau$ over the range 180–5000. The wall-pressure fluctuation PSD computed from the net source CSD using (3.9) agrees with that obtained directly from the solver (figure 1*a*) for both $Re_\tau$ (not shown). We will investigate the distribution of the net sources that give rise to this premultiplied PSD peak in the next section.

To identify the range of −5 decay in the power and streamwise wavenumber spectrum, we plot the diagnostic functions $(\omega\nu/u_\tau^2)^5\phi_{pp}(\omega)u_\tau^2/(\tau_w^2\nu)$ and $(k_1\nu/u_\tau)^5\phi_{pp}(k_1)u_\tau/(\tau_w^2\nu)$ in figures 3(*a*) and 3(*b*), respectively. The function is constant in the range of −5 slope. The diagnostic function does not return a significant range of frequency and wavenumbers that show −5 decay. We observe a constant value (indicated by the dashed-dotted horizontal line) for only a very small range of frequencies and wavenumbers. To observe the decay in a significant range, we require higher Reynolds numbers.

The wall-pressure wavenumber spectra show a low-wavenumber peak around $k_1\delta \approx 3$ for both $Re_\tau = 180$ and 400, respectively, when the $y$-axis is plotted in linear coordinates (figure 4*a*). This corresponds to streamwise wavelengths $\lambda_1/\delta$ of $\sim$2. Such low-wavenumber peaks in the range $k_x\delta \approx 2.5$–$3.4$ ($\lambda_x/\delta \approx 1.8$–$2.4$) have been previously observed by Abe *et al.* (2005) and Panton *et al.* (2017) in a turbulent channel for friction Reynolds numbers ranging from 180 to 5000. We observe the corresponding low-frequency peak in the wall-pressure PSD at $\omega\delta/u_\tau = 37.6$ and 50.2 for $Re_\tau = 180$ and 400, respectively (shown in figure 4*b*). Later, we identify the decorrelated fluid sources responsible for this low-frequency peak in the PSD using spectral POD and relate this to the observations of Abe *et al.* (2005).

Figure 4(*c*) shows the spanwise wavenumber spectrum of the wall-pressure fluctuations in inner units. The spectrum at $Re_\tau = 180$ agrees well with Choi & Moin (1990). Therefore, the spanwise resolution is sufficient enough to resolve the fine scale spanwise features of wall-pressure fluctuations.

### 4.2. *Wall-pressure source distribution analysis*

The wall-parallel plane that contributes the most to the wall-pressure PSD can be determined from the real part of the wall-pressure fluctuation – net source CSD

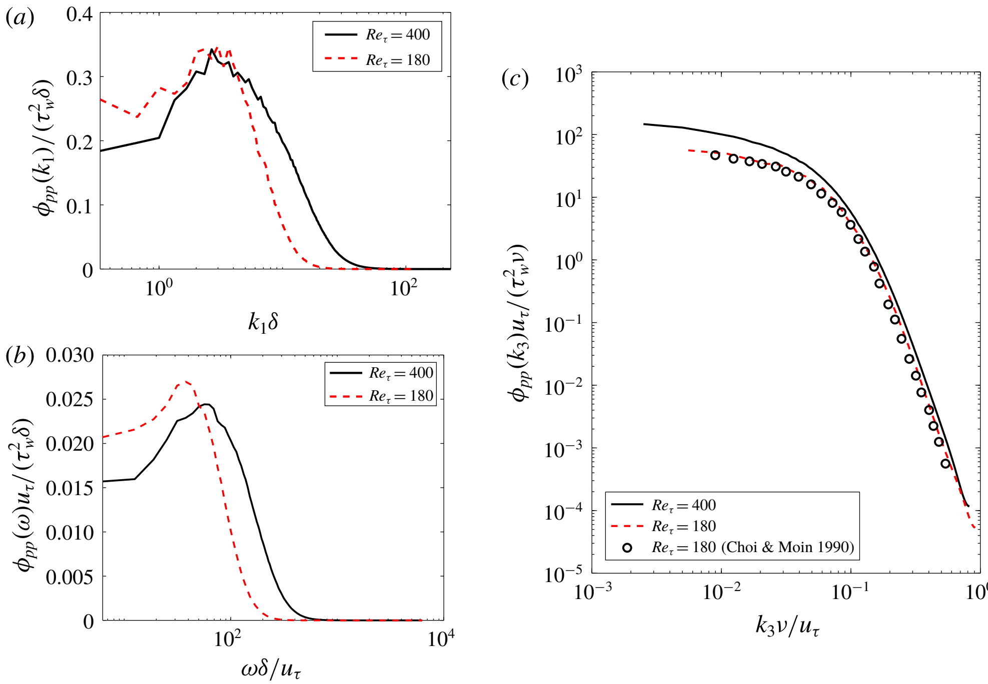


FIGURE 4. (*a*) Wall-pressure fluctuation streamwise wavenumber spectrum with linear *y*-axis. (*b*) Wall-pressure fluctuation PSD with linear *y*-axis. (*c*) Wall-pressure fluctuation spanwise wavenumber spectrum in inner units.

$\Psi(y^+, \omega^+)$ (defined in § 3.1). Figure 5(*a*) shows the wall-pressure fluctuation – net source CSD in premultiplied form normalized by the root mean square (r.m.s.) of the wall-pressure fluctuations $(y^+\omega^+ Re(\Psi^+(y^+, \omega^+))/\langle p^2\rangle^+)$; $y^+$ is the distance from the wall in viscous units. The coordinates $(\omega_p^+, y_p^+)$ of the peak value in the contours are (0.35, 16.5) and (0.35, 18.4) for $Re_\tau = 180$ and 400, respectively. The frequency coordinate of the peak in the contour levels $(\omega^+ = 0.35)$ is the same as the premultiplied power spectrum peak location shown in figure 1(*b*). Therefore, the corresponding wall-normal coordinate yields the location of the wall-parallel plane that contributes the most to the premultiplied power spectrum peak. Specifically, it is the cross-correlation with this dominant plane that contributes the most. This coincidence is not surprising since integrating figure 5(*a*) in the wall-normal direction yields figure 1(*b*) (normalized by $\langle p^2\rangle$). The wall-normal coordinate of the peak indicates that it is the correlations with the buffer region that contribute the most to the wall-pressure PSD at the Reynolds numbers considered.

Even though the peak location differs slightly in inner units for the two $Re_\tau$, the main implication of this result is that the peak lies in the buffer region. Further, we cannot expect the same location of the peak for both $Re_\tau$. This is because the real part of the peak wall-pressure fluctuation – net source CSD includes the contribution from the correlations with the rest of the channel (since $\Psi(y_p^+, \omega) = \int_{-\delta}^{+\delta} \Gamma(y_p^+, y', \omega)\, \mathrm{d}y'$) and not just the inner layer. Therefore, the peak need not necessarily scale in inner units. We believe that changing the Reynolds number would not affect this main finding. We expect the peak value of wall-pressure fluctuation – net source CSD to still occur in the buffer layer.

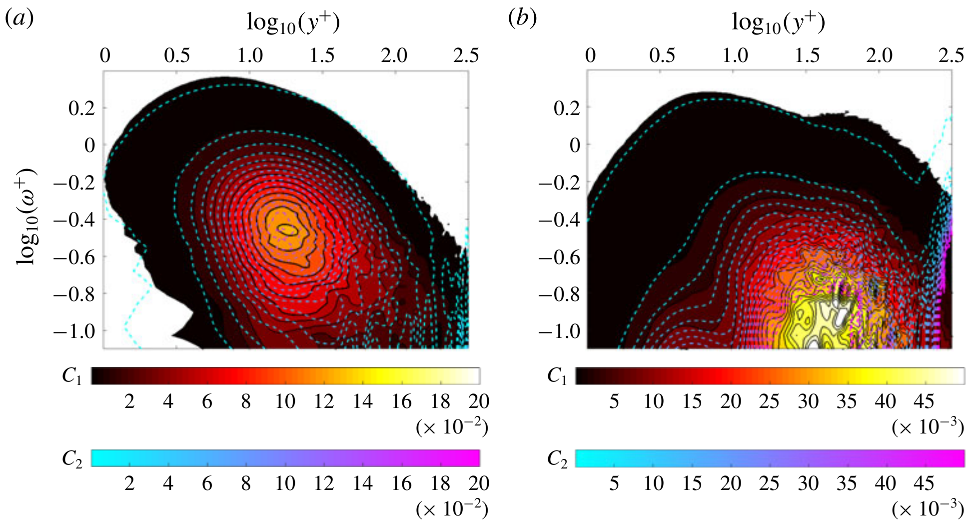


FIGURE 5. (*a*) Real part of premultiplied wall-pressure fluctuation – net source CSD $(y^+\omega^+ Re(\Psi(y^+,\ \omega^+))/\langle p^2\rangle)$ for $Re_\tau = 400$ (black solid lines with filled contours with colour map $C_1$) and 180 (line contours with colour map $C_2$). Contour lines are 20 equally spaced values between $4\times10^{-4}$ and $2\times10^{-1}$. (*b*) Premultiplied net source PSD $(y^+\omega^+\Gamma(y^+, y^+, \omega^+)/\langle\Gamma^2\rangle)$ for $Re_\tau = 400$ (black solid lines with filled contours with colour map $C_1$) and 180 (line contours with colour map $C_2$). Contour lines are 20 equally spaced values between $4\times10^{-5}$ and $5\times10^{-2}$.

The phase difference between the wall-pressure and the dominant net source obtained from the argument of $\Psi(y_p^+,\ \omega_p^+)$ is $0.013\pi$ and $0.016\pi$ for $Re_\tau = 180$ and 400 respectively, is very small. Hence, the dominant net sources and the wall-pressure fluctuation are in phase with each other. The contour levels of the normalized wall-pressure fluctuation – net source CSD plotted in figure 5(*a*) almost overlap in the range $\omega^+ > 0.3 \sim 10^{-0.5}$. This indicates that the high-frequency contribution to the r.m.s. scales in inner units. However, in the near-wall region ($y^+ < 10$), the overlap in the contours is observed for a much larger frequency range $\omega^+ > 0.16 \sim 10^{-0.8}$. This implies that for most of the frequency range, the contribution to wall-pressure PSD from the near-wall region scales in inner units.

Next, we investigate whether the net source PSD can be used to infer the location of the dominant source of wall-pressure fluctuation instead of the wall-pressure fluctuation – net source CSD. Figure 5(*b*) shows the contours of the premultiplied net source PSD $\Gamma(y^+, y^+, \omega^+)$ in fractional form for both $Re_\tau$. The main contribution to the net source PSD is seen to be from the region around $y^+ \approx 30$ and at frequencies much lower than $\omega^+ \approx 0.35$. There is no signature of the distinct premultiplied peak observed in figure 5(*a*). From visual inspection at low frequencies ($\omega^+ < 1$), the shape of the contours in figure 5(*b*) do not have similar shape to those in figure 5(*a*). However, at high frequencies $\omega^+ > 1$, we observe from figure 6(*a*,*b*) that the contour shapes near the wall ($y^+ < 30$) are almost identical. Therefore, the net source PSD $\Gamma(y^+,\ y^+,\ \omega^+)$ is a good proxy for wall-pressure fluctuation – net source CSD $\Psi(y^+,\ \omega^+)$ at high frequencies to obtain the pattern of the net sources. The reason for this behaviour can be understood from the near-wall contours of the real part of the net source CSD shown in figure 7. Figures 7(*a*) and 7(*b*) show the contours at frequencies $\omega^+ = 0.35$ and $\omega^+ = 1$, respectively, for $Re_\tau = 180$. Clearly, the

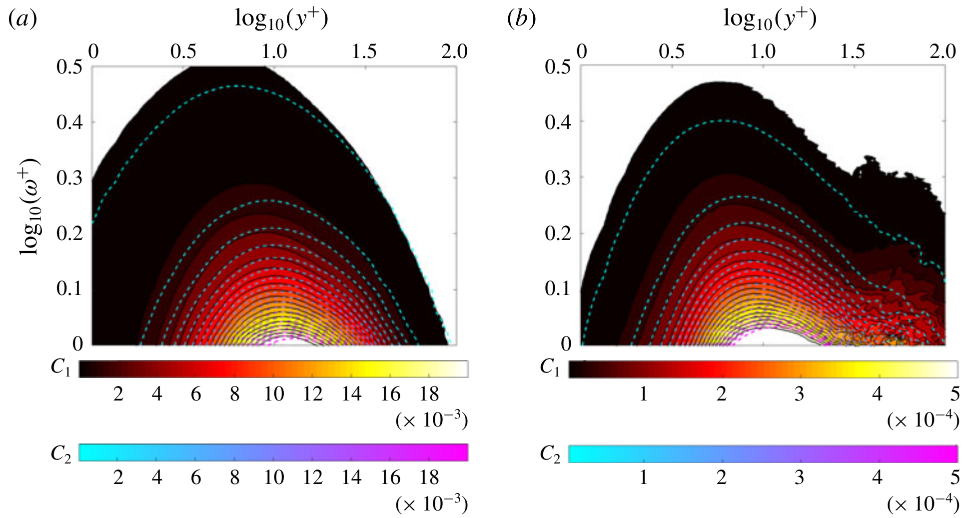


FIGURE 6. ($a$) Real part of the high-frequency premultiplied wall-pressure fluctuation – net source CSD ($y^+\omega^+ Re(\Psi(y^+, \omega^+))/\langle p^2\rangle$) for $Re_\tau = 400$ (black solid lines with filled contours with colour map $C_1$) and 180 (line contours with colour map $C_2$). Contour lines are 20 equally spaced values between $4\times 10^{-5}$ and $2\times 10^{-2}$. ($b$) High-frequency premultiplied fractional net source power spectral density $y^+\omega^+\Gamma(y^+, y^+, \omega^+)/\langle \Gamma^2\rangle$ for $Re_\tau = 400$ (black solid lines with filled contours with colour map $C_1$) and 180 (line contours with colour map $C_2$). Contour lines are 20 equally spaced values between $4\times 10^{-6}$ and $2\times 10^{-2}$.

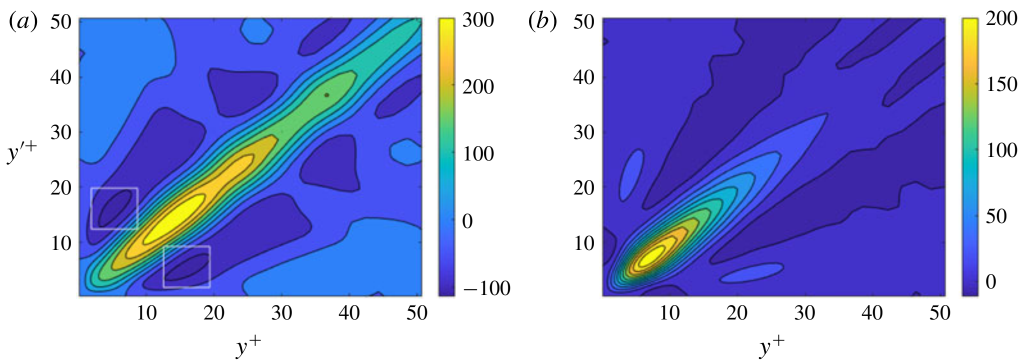


FIGURE 7. Real part of $\Gamma(r, s, \omega)$ (normalized by $\phi_{pp}(\omega)$) at ($a$) $\omega^+ \approx 0.35$ and ($b$) $\omega^+ \approx 1$ for $Re_\tau = 180$.

low-frequency ($\omega^+ = 0.35$) contours show a large negatively cross-correlated region around $(y^+, y'^+) = (5, 15)$ (shown by white boxes). These dominant negative regions found at low frequencies contribute to the wall-pressure fluctuation – net source CSD (3.10) leading to different shapes compared to the net source PSD. However, such negative regions are not present at the higher frequency $\omega^+ = 1$. Therefore, the wall-pressure fluctuation – net source CSD and the net source CSD have similar shapes near to the wall at high frequencies.

The wall-pressure fluctuation – net source CSD (normalized with wall-pressure PSD) is plotted in premultiplied form for selected frequencies between $\omega^+ = 0.35$

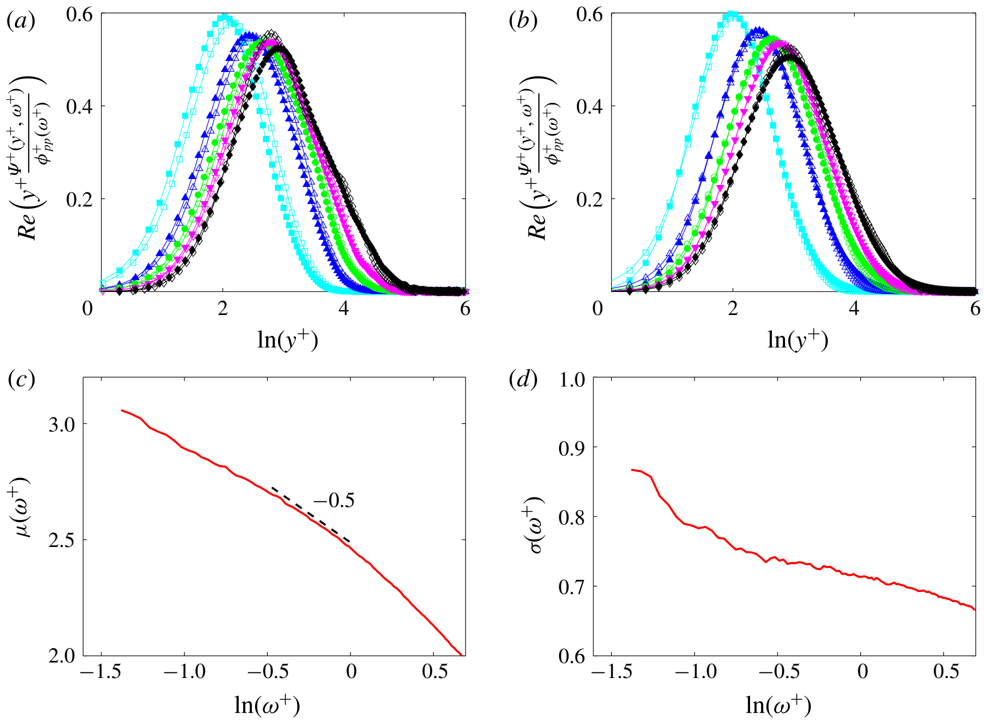


FIGURE 8. ($a$) Premultiplied wall-pressure fluctuation – net source CSD ($y^+\Psi^+(y^+,\ \omega^+)/\phi^+_{pp}(\omega^+)$) at different frequencies for $Re_\tau = 180$ (empty markers) and 400 (filled markers). ($b$) Comparison of fitted log-normal Gaussians (filled markers) to the wall-pressure fluctuation – net source for $Re_\tau = 400$ (empty markers). ($c$) Variation of mean $\mu(\omega^+)$ and ($d$) standard deviation $\sigma(\omega^+)$ of the fitted log-normal profile for $Re_\tau = 400$. ◇, ◆: $\omega^+ \approx 0.35$, ▽, ▼: $\omega^+ \approx 0.5$, ○, ●: $\omega^+ \approx 0.7$, △, ▲: $\omega^+ \approx 1$, □, ■: $\omega^+ \approx 2$.

and $\omega^+ = 2$ in figure 8($a$). Due to the normalization, each profile has unit area under it. From the figure, we can observe that the curves for $Re_\tau = 180$ and 400 are very close to each other for the different frequencies plotted. Further, visual inspection shows that we can model the profiles using log-normal function in $y^+$. Therefore, normalized log-normal profiles of the form

$$f(y^+,\omega^+) = \frac{1}{\sigma(\omega^+)\sqrt{2\pi}} \exp\left(-\left(\frac{\ln(y^+) - \mu(\omega^+)}{\sqrt{2}\sigma(\omega^+)}\right)^2\right) \tag{4.1}$$

are fitted to the $Re_\tau = 400$ data for different $\omega^+$ using a nonlinear least squares fit and plotted in figure 8($b$).

The mean and standard deviation of the fitted log-normal curves characterize the location and the width of the dominant net source respectively as a function of frequency. The correlation between the planes contained in this width have a sizeable contribution to wall-pressure PSD. Figures 8($c$) and 8($d$) show the mean ($\mu(\omega^+)$) and standard deviation ($\sigma(\omega^+)$) as a function of frequency respectively. We define the location of the dominant net source $y_p^+(\omega^+)$ as $y_p^+(\omega^+) = \exp(\mu(\omega^+))$. From figure 8($c$), we observe that the location of the dominant net source moves closer to the wall with increase in frequency through a power law dependence $y_p^+ \sim (\omega^+)^m$. The

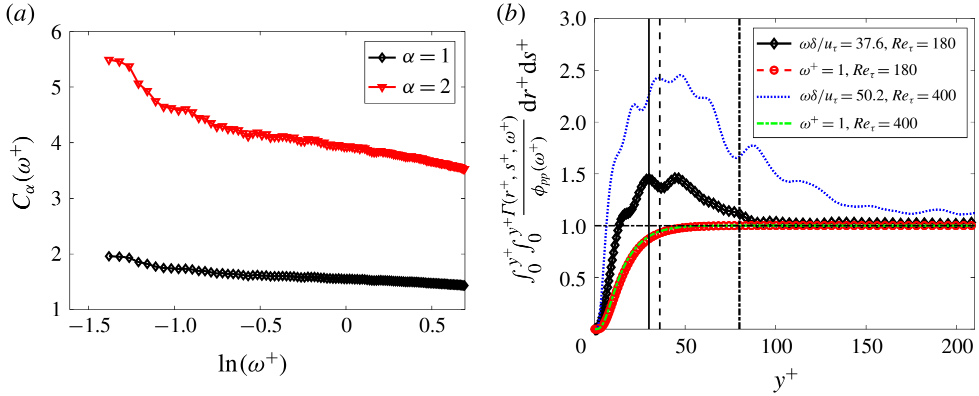


FIGURE 9. ($a$) Variation of $C_\alpha(\omega^+)$ for $Re_\tau = 400$. ($b$) Partial wall-pressure fluctuation spectra from sources that extend from the wall to a particular $y^+$ for $Re_\tau = 180$ and 400 in near-wall region. The vertical solid, dashed, dash-dotted lines denote $y^+ = 30$, $y/\delta = 0.2$ for $Re_\tau = 180$ and $y/\delta = 0.2$ for $Re_\tau = 400$, respectively. The horizontal dash-dotted line denotes partial contribution equal to 1.

value of $m$ depends on the frequency range. In the low $(-1.5 < \ln(\omega^+) < 0.5)$, mid $(-0.5 < \ln(\omega^+) < 0)$ and high $(\omega^+ > 1)$ frequency range, the value of the exponent $m$ is larger than $-0.5$, equal to $-0.5$ and smaller than $-0.5$ respectively.

Figure 8($d$) shows that the standard deviation of the log-normal profiles decreases with increasing frequency. We use the standard deviation profile to show that for $\omega^+ > e^{-1}$, the width of the dominant net source is proportional to its location. We define the wall-normal width of the net source $\Delta y^+(\omega^+; \alpha, \sigma)$ as

$$\Delta y^+(\omega^+; \alpha, \sigma) = y^+_{max}(\omega^+; \alpha, \sigma) - y^+_{min}(\omega^+; \alpha, \sigma), \tag{4.2}$$

where $y^+_{max}$, $y^+_{min}$ and $y^+_p$ are related as

$$\left.\begin{aligned} \ln(y^+_{max}(\omega^+; \alpha, \sigma)) - \ln(y^+_{min}(\omega^+; \alpha, \sigma)) &= 2\alpha\sigma(\omega^+), \\ \ln(y^+_p(\omega^+)) - \ln(y^+_{min}(\omega^+; \alpha, \sigma)) &= \alpha\sigma(\omega^+). \end{aligned}\right\} \tag{4.3}$$

The parameter $\alpha$ is the proportion of the standard deviation used to define the width of the net source. Using the above expressions, the width $\Delta y^+(\omega^+; \alpha, \sigma)$ can be shown to be

$$\left.\begin{aligned} \Delta y^+(\omega^+; \alpha, \sigma) &= C(\omega^+; \alpha, \sigma) y^+_p(\omega^+), \\ C(\omega^+; \alpha, \sigma) &= (\mathrm{e}^{\alpha\sigma(\omega^+)} - \mathrm{e}^{-\alpha\sigma(\omega^+)}). \end{aligned}\right\} \tag{4.4}$$

The variation of $C_\alpha(\omega^+)$ for $\alpha = 1, 2$ using $Re_\tau = 400$ data is shown in figure 9($a$). The proportionality constant is observed to vary slowly for $\omega^+ > \ln(-1)$. Hence, in this frequency range, the width of the dominant net source is proportional to its location.

The contribution of the interaction between the net sources in the inner and overlap/outer region to wall-pressure PSD can be investigated using the wall-pressure fluctuation – net source CSD. Figure 9($b$) shows the partial contribution (normalized by the wall-pressure PSD) $\int_0^{y^+} \int_0^{y^+} \varGamma(r^+, s^+, \omega^+)/\phi_{pp}(\omega^+)\mathrm{d}r^+\mathrm{d}s^+$ from the net sources contained between the wall and a given $y^+$ for two selected frequencies. At the low-frequency wall-pressure linear PSD peak (which is $\omega\delta/u_\tau = 37.6$ and $\omega\delta/u_\tau = 50.2$

for $Re_\tau = 180$ and 400, respectively), we observe that the partial contribution first increases and then decreases. However, a monotonically increasing behaviour is observed for the high frequency. In order to investigate the implication of the non-monotonic low-frequency behaviour, we split the domain $0 < y/\delta < 1$ into an inner region $0 < y^+ < 30$, an outer/overlap region $30 < y^+ < Re_\tau$. The contribution to wall-pressure PSD from sources within $y/\delta = 1$ can then be accordingly split as

$$\begin{aligned}&\int_0^{Re_\tau}\int_0^{Re_\tau}\frac{\Gamma(r^+,s^+,\omega^+)}{\phi_{pp}(\omega^+)}\,\mathrm{d}r^+\,\mathrm{d}s^+\\&\quad=\int_0^{30}\int_0^{30}\frac{\Gamma(r^+,s^+,\omega^+)}{\phi_{pp}(\omega^+)}\,\mathrm{d}r^+\,\mathrm{d}s^+ + \int_{30}^{Re_\tau}\int_{30}^{Re_\tau}\frac{\Gamma(r^+,s^+,\omega^+)}{\phi_{pp}(\omega^+)}\,\mathrm{d}r^+\,\mathrm{d}s^+\\&\qquad+2Re\left(\int_0^{30}\int_{30}^{Re_\tau}\frac{\Gamma(r^+,s^+,\omega^+)}{\phi_{pp}(\omega^+)}\,\mathrm{d}r^+\,\mathrm{d}s^+\right).\end{aligned} \tag{4.5}$$

From figure 9(*b*), we observe that at the lower frequency, this contribution from sources within $y/\delta = 1$ is smaller than the inner region contribution $\int_0^{30}\int_0^{30}(\Gamma(r^+,s^+,\omega^+)/\phi_{pp}(\omega^+))\,\mathrm{d}r^+\,\mathrm{d}s^+$. Therefore,

$$\int_{30}^{Re_\tau}\int_{30}^{Re_\tau}\frac{\Gamma(r^+,s^+,\omega^+)}{\phi_{pp}(\omega^+)}\,\mathrm{d}r^+\,\mathrm{d}s^+ \leqslant -2Re\left(\int_0^{30}\int_{30}^{Re_\tau}\frac{\Gamma^+(r^+,s^+,\omega^+)}{\phi_{pp}(\omega^+)}\,\mathrm{d}r^+\,\mathrm{d}s^+\right). \tag{4.6}$$

Note the left-hand side of the above inequality is a positive real number. This indicates that (i) the contribution from the cross-correlations between the inner and the overlap/outer region dominates the contribution from the outer/overlap region alone, (ii) the phase difference between the net sources in these two regions is predominantly in the range $\pi/2$ to $\pi$ or $-\pi$ to $-\pi/2$. In other words, a positive (or negative) low-frequency event in the near-wall region is predominantly correlated with a negative (or positive) low-frequency event in the overlap/outer region. Therefore, the observed non-monotonic behaviour at low frequencies implies a dominant interaction between the net sources in the inner and outer regions of the channel at such frequencies. Such inner–outer interaction at long streamwise wavelengths has been previously observed for the streamwise velocity fluctuations by Del Álamo & Jiménez (2003) and Morrison (2007), and is the reason for the mixed scaling (De Graaff & Eaton 2000) of the streamwise velocity r.m.s. peak in wall-bounded flows.

We further investigate the fractional contributions of the wall-pressure sources in the inner ($y^+ < 30$), overlap ($30 < y^+ < 0.2Re_\tau$) and outer regions ($0.2 < y/\delta < 1$) and their cross-correlations to the wall-pressure PSD by splitting $\int_0^{Re_\tau}\int_0^{Re_\tau}(\Gamma(r^+,s^+,\omega^+)/\phi_{pp}(\omega^+))\,\mathrm{d}r^+\,\mathrm{d}s^+$ into the sum,

$$\begin{aligned}\int_0^{Re_\tau}\int_0^{Re_\tau}\frac{\Gamma(r^+,s^+,\omega^+)}{\phi_{pp}(\omega^+)}\,\mathrm{d}r^+\,\mathrm{d}s^+ &= \underbrace{\int_0^{30}\int_0^{30}\frac{\Gamma(r^+,s^+,\omega^+)}{\phi_{pp}(\omega^+)}\,\mathrm{d}r^+\,\mathrm{d}s^+}_{C_{11}}\\&+\underbrace{\int_{30}^{0.2Re_\tau}\int_{30}^{0.2Re_\tau}\frac{\Gamma(r^+,s^+,\omega^+)}{\phi_{pp}(\omega^+)}\,\mathrm{d}r^+\,\mathrm{d}s^+}_{C_{22}}+\underbrace{\int_{0.2Re_\tau}^{Re_\tau}\int_{0.2Re_\tau}^{Re_\tau}\frac{\Gamma(r^+,s^+,\omega^+)}{\phi_{pp}(\omega^+)}\,\mathrm{d}r^+\,\mathrm{d}s^+}_{C_{33}}\end{aligned}$$

| Term | $Re_\tau = 180$ | | $Re_\tau = 400$ | |
|---|---|---|---|---|
| | $\dfrac{\omega\delta}{u_\tau} = 36.7$ | $\omega^+ = 1$ | $\dfrac{\omega\delta}{u_\tau} = 50.2$ | $\omega^+ = 1$ |
| $C_{11}$ | 1.45 | 0.87 | 2.3 | 0.9 |
| $C_{22}$ | 0.67 | 0.02 | 3.03 | 0.04 |
| $C_{33}$ | 0.87 | 0.02 | 1.08 | 0.001 |
| $2Re(C_{12})$ | −0.76 | 0.038 | −3.65 | 0.06 |
| $2Re(C_{23})$ | −0.44 | 0.005 | −1.83 | −0.003 |
| $2Re(C_{31})$ | −0.76 | 0.039 | 0.09 | 0.0006 |

TABLE 2. Fractional contributions of the inner, overlap and outer regions to the wall-pressure fluctuation PSD. For definitions of $C_{11}$, $C_{22}$, $C_{33}$, $C_{12}$, $C_{23}$ and $C_{31}$, see (4.7).

$$
+\,2Re\left(\underbrace{\int_0^{30}\int_{30}^{0.2Re_\tau}\frac{\varGamma(r^+,s^+,\omega^+)}{\phi_{pp}(\omega^+)}\,\mathrm{d}r^+\,\mathrm{d}s^+}_{C_{12}}+\underbrace{\int_{30}^{0.2Re_\tau}\int_{0.2Re_\tau}^{Re_\tau}\frac{\varGamma(r^+,s^+,\omega^+)}{\phi_{pp}(\omega^+)}\,\mathrm{d}r^+\,\mathrm{d}s^+}_{C_{23}}\right.
$$

$$
\left.+\underbrace{\int_{0.2Re_\tau}^{Re_\tau}\int_0^{30}\frac{\varGamma(r^+,s^+,\omega^+)}{\phi_{pp}(\omega^+)}\,\mathrm{d}r^+\,\mathrm{d}s^+}_{C_{31}}\right). \tag{4.7}
$$

Table 2 shows the value of each term on the right-hand side of the above equation at the two $Re_\tau$ for the same frequencies chosen in figure 9(*b*). For the lower frequency, we observe that the magnitude of the contribution from the cross-correlations between the regions is comparable to the contribution within the regions. However, at high frequency, the contribution within each region dominates over the cross-correlation between the regions. The real part of the cross-correlations is negative at the lower frequency for $Re_\tau = 180$. As discussed in the previous paragraph, this implies that the phase difference of the wall-pressure sources in the different regions lie in the range $\pi/2$ to $\pi$ or $-\pi/2$ to $-\pi$. For the higher $Re_\tau$, except the inner and outer regions ($2Re(C_{31})$), the phase difference between all the other regions lies in the same range as the lower $Re_\tau$. Overall, we observe that the cross-correlations between the wall-pressure sources present in the inner, overlap and outer regions are important contributors to the PSD at low frequency but not at high frequency.

Further, this framework can be used to identify the location of the dominant sources that lead to the $\omega^{-1}$ behaviour of the wall-pressure PSD in the mid-frequency range (observed at very high Reynolds numbers). Farabee & Casarella (1991) noted that the $\omega^{-1}$ behaviour is responsible for the logarithmic dependence of the wall-pressure r.m.s. on Reynolds number (Abe *et al.* 2005; Hu *et al.* 2006; Jimenez & Hoyas 2008).

### 4.3. *Spectral POD of net source CSD*

Before we investigate the spectral POD modes of the net source CSD, we first examine the relevance of the modes to wall-pressure fluctuation. We can decompose the wall-pressure fluctuation $p(x, 0, z, t)$ at a typical point $(x, z)$ on the wall by expressing its Fourier transform $\hat{p}(x, 0, z, \omega)$ (equation (3.5)) in terms of the spectral

POD modes. We have

$$p(x,0,z,t)=\int_{-\infty}^{+\infty}\hat{p}(x,0,z,\omega)\mathrm{e}^{\mathrm{i}\omega t}\,\mathrm{d}\omega, \tag{4.8}$$

$$p(x,0,z,t)=\int_{-\infty}^{+\infty}\left(\int_{-\delta}^{+\delta}\hat{f}_G(x,y,z,\omega)\,\mathrm{d}y\right)\mathrm{e}^{\mathrm{i}\omega t}\,\mathrm{d}\omega. \tag{4.9}$$

We use the decomposition in (3.18) to express $\hat{f}_G(x, y, z, \omega)$ in terms of the spectral POD modes and obtain

$$p(x,0,z,t)=\int_{-\infty}^{+\infty}\sum_{j=1}^{\infty}\alpha_i(x,z,\omega)\left(\int_{-\delta}^{+\delta}\Phi_j^*(y,\omega)\,\mathrm{d}y\right)\mathrm{e}^{\mathrm{i}\omega t}\,\mathrm{d}\omega. \tag{4.10}$$

Rearranging the integral and writing $\Phi_j(y, \omega)$ as $|\Phi_j(y, \omega)|\mathrm{e}^{-\mathrm{i}\angle\Phi_j(y,\omega)}$, we obtain

$$p(x,0,z,t)=\int_{-\delta}^{+\delta}\int_{-\infty}^{+\infty}\sum_{j=1}^{\infty}\alpha_j(x,z,\omega)|\Phi_j(y,\omega)|\mathrm{e}^{\mathrm{i}(-\angle\Phi_j(y,\omega)+\omega t)}\,\mathrm{d}\omega\,\mathrm{d}y. \tag{4.11}$$

The above equation expresses the wall-pressure fluctuation as a contribution from each spectral POD mode. Recall that the individual contributions are decorrelated, i.e. $\langle\alpha_i(x, z, \omega)\alpha_j^*(x, z, \omega_o)\rangle = \lambda_i(\omega)\delta_{ij}\delta(\omega-\omega_o)$, where $\delta$ is the Dirac delta function. Note that, since we integrate over all wavenumbers, the contribution of coherent structures of all length scales is included.

The wall-normal phase velocity of the net sources represented by the $i$th spectral POD mode can be quantified as a function of the wall-normal distance using the phase $\angle\Phi_i(y, \omega)$. We define a local wall-normal phase velocity $c_i^+(y^+, \omega^+)$ in viscous units as

$$c_i^+(y^+,\omega^+)=\omega^+/k_i^+(y^+,\omega^+), \tag{4.12}$$

where the local wavenumber $k_i^+(y^+, \omega^+)$ is defined as $k_i^+(y^+, \omega^+) = \partial\angle\Phi_i(y^+, \omega^+)/\partial y^+$. Note that a negative phase velocity indicates an enclosed wave travelling towards the wall and *vice versa*. Also, this is similar to estimating the instantaneous frequency of a temporal signal using Hilbert transform (Huang & Shen 2014).

We found that, for a wide range of frequencies, setting $\beta$ (3.16) to 0.1 gives a dominant spectral POD mode ($\Phi_1$) that contributes to all of the wall-pressure PSD (see figure 10). This observation is consistent with the discussion after (3.20). Note that the lowest frequency in figure 10 corresponds to the low-frequency peak in the linear PSD. Also, $\omega^+ = 0.35$ is the location of the premultiplied PSD peak. Therefore, the dominant modes at these peak frequencies represent the decorrelated source responsible for the peaks.

Further, the dominant mode represents the active part of the net source Fourier transform ($\hat{f}_G(x, y, z, \omega)$). It is active in the sense that it contributes to the entire PSD. The remaining portion of $\hat{f}_G(x, y, z, \omega)$ is inactive in the sense that it does not contribute to the wall-pressure PSD. The suboptimal spectral POD modes comprise this inactive portion. Essentially, the contribution of the suboptimal modes from different wall-normal locations undergo destructive interference resulting in zero net contribution. Since the active and inactive parts of $\hat{f}_G(x, y, z, \omega)$ stem from different modes, they are decorrelated.

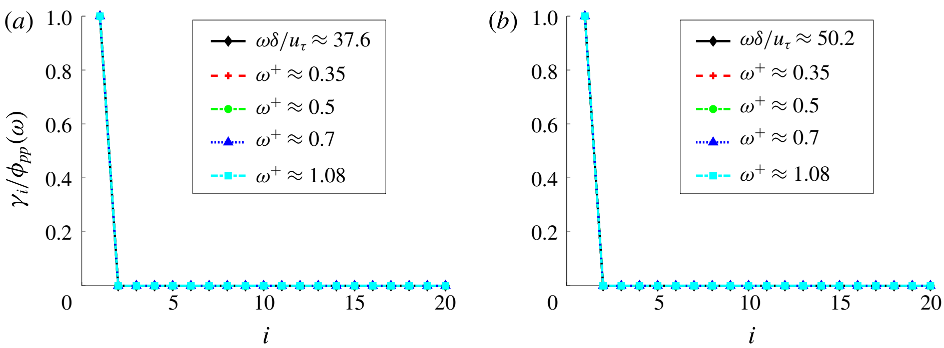


FIGURE 10. Fractional contribution of the first 20 spectral POD modes computed using the Poisson inner product ($\beta = 0.1$) to the wall-pressure PSD for (*a*) $Re_\tau = 180$ and (*b*) $Re_\tau = 400$ at different frequencies.

Separating the active and inactive parts of $\hat{f}_G(x, y, z, \omega)$ in (3.18), we have

$$\left.\begin{aligned} \hat{f}_g(x, y, z, \omega) &= \alpha_1(x, z, \omega)\Phi_1^*(y, \omega) + I(x, y, z, \omega), \\ I(x, y, z, \omega) &= \sum_{j=2}^{\infty} \alpha_j(x, z, \omega)\Phi_j^*(y, \omega), \end{aligned}\right\} \tag{4.13}$$

where $\alpha_1(x, z, \omega)\Phi_1^*(y, \omega)$ and $I(x, y, z, \omega)$ are the active and inactive portions of $\hat{f}_G(x, y, z, \omega)$, respectively. Correlating the two, we obtain

$$\begin{aligned} \langle \alpha_1^*(x, z, \omega)\Phi_1(r, \omega)I(x, s, z, \omega_o)\rangle &= \sum_{j=2}^{\infty} \langle \alpha_1^*(x, z, \omega)\alpha_j(x, z, \omega)\rangle \Phi_1(r, \omega)\Phi_j^*(s, \omega_o) \\ &= \sum_{j=2}^{\infty} \lambda_1 \delta_{j1} \Phi_1(r, \omega)\Phi_j^*(s, \omega_o) \text{ (using (3.18))} \\ &= 0. \end{aligned} \tag{4.14}$$

Therefore, both parts are decorrelated. Note that $I(x, y, z, \omega)$, the inactive part, is orthogonal to the eigenfunction $\bar{\Phi}_1^*(y, \omega)$ (equation (3.15)) in the $L^2$ inner product. Decreasing $\beta$ to even smaller values does not affect the mode shape or the eigenvalues for the frequencies in figure 10.

Since we use a Poisson inner product, the dominant spectral POD mode need not be energetically dominant. In other words, it need not contribute the most to the integrated net source PSD ($\int_{-\delta}^{+\delta} \Gamma(r, r, \omega)\,\mathrm{d}r$). Figure 11 shows this behaviour for low frequencies. In the figure, $\bar{\lambda}_j(\omega) = \lambda_j(\omega)|\int_{-\delta}^{+\delta} \Phi_j(y, \omega)\,\mathrm{d}y|^2$ is the contribution of the $j$th mode to the integrated PSD. We observe that the fractional contribution of the dominant mode increases with frequency. At $\omega^+ = 1$, the dominant spectral POD mode is the energetically dominant mode.

Figure 12 shows the wall-normal variation of the envelope and phase of the dominant mode at the premultiplied spectrum peak $\omega^+ = 0.35$ and a few higher frequencies $\omega^+ = 0.5$, 0.7 and 1. The dominant modes have a similar shape in inner units for both $Re_\tau$. Its envelope (figure 12*a*,*c*) represents sources confined near the wall with intensities peaking in the buffer layer. With increasing frequency, the

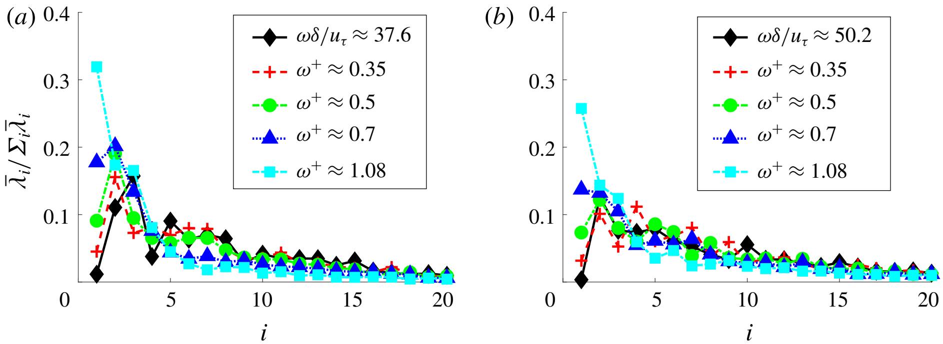


FIGURE 11. Fractional contribution of the first 20 spectral POD modes computed using the Poisson inner product ($\beta = 0.1$) to the integrated net source PSD for (*a*) $Re_\tau = 180$ and (*b*) $Re_\tau = 400$ at different frequencies.

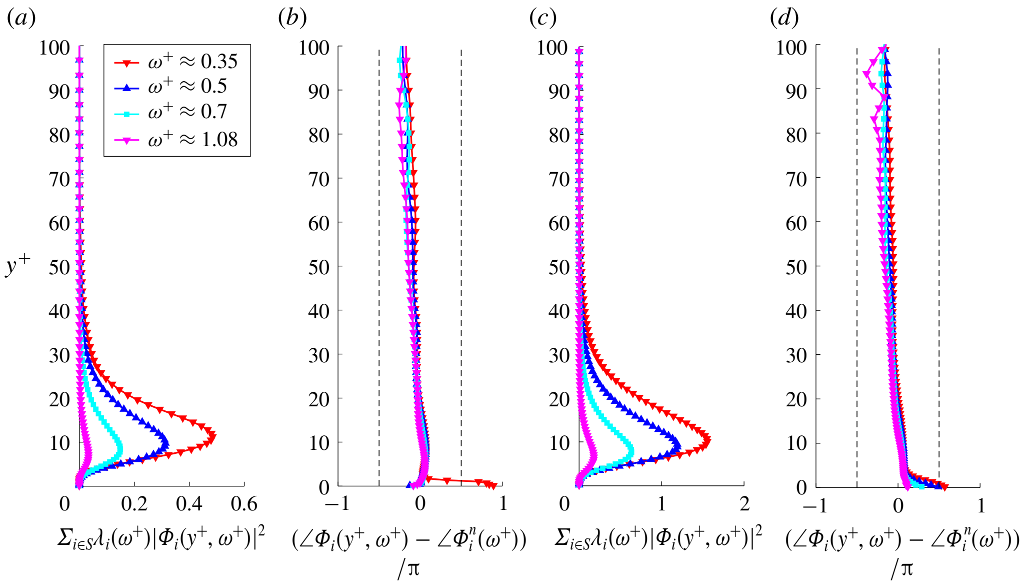


FIGURE 12. Envelope (*a*,*c*) and phase (*b*,*d*) of the dominant spectral POD mode computed using the Poisson inner product ($\beta = 0.1$) for a few selected high frequencies. Panels (*a*,*b*) and (*c*,*d*) are for $Re_\tau = 180$ and 400, respectively. The left and right dashed black solid line in (*b*,*d*) indicate $\angle\Phi_i(y^+,\omega^+) - \angle\Phi_i^n(\omega^+)$ equal to $-\pi/2$ and $\pi/2$, respectively.

wall-normal location of the peak moves closer to the wall, and the width of the envelope decreases. This behaviour of the dominant mode is consistent with that of the wall-pressure fluctuation – net source CSD. The phase (figure 12*b*,*d*) of the dominant mode varies between $-\pi/2$ and $\pi/2$. Therefore, the contributions from different wall-normal locations undergo constructive interference. Further, the phase variation is almost linear with a negative slope, at least around the envelope peak. The negative slope indicates that the envelope encloses a wave travelling towards the wall.

Figures 13(*a*) and 13(*b*) show the magnitude and phase, respectively, of the dominant spectral POD mode at the low-frequency linear PSD peak (figure 4).

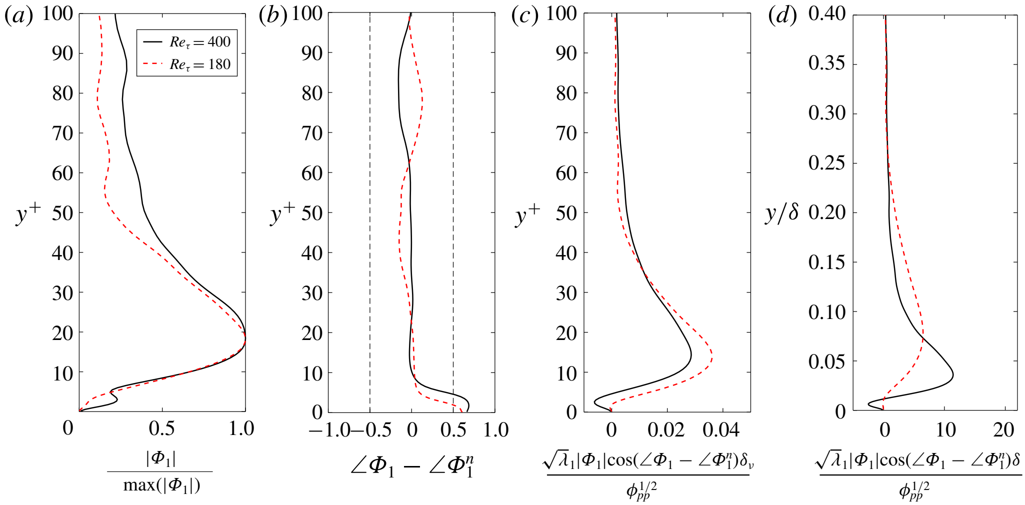


FIGURE 13. Envelope (*a*) and phase (*b*) of the dominant spectral POD mode computed using the Poisson inner product at the low-frequency linear PSD peak. Panels (*c*,*d*) show the normalized wall-normal contribution of the dominant mode to the wall-pressure PSD in inner and outer units, respectively.

Recall that the frequencies are $\omega\delta/u_\tau = 37.6$ for $Re_\tau = 180$ and 50.2 for $Re_\tau = 400$. The envelope of the dominant mode peaks around $y^+ \approx 15$ for both $Re_\tau$. The phase variation does not show any noticeable slope indicating that the different wall-normal locations are in phase with each other, at least around the envelope peak.

In figures 13(*c*) and 13(*d*), we show the wall-normal contribution of the dominant mode to the wall-pressure PSD in inner and outer units, respectively. The curves are normalized to obtain unit integral along the *y*-axis. The contribution peaks at $y^+ \approx 15$ for both $Re_\tau$. Also, figure 13(*c*) shows a negative contribution close to the wall for $Re_\tau = 400$ that is not present for $Re_\tau = 180$. We observe that the region $y^+ > 30$ contributes more for the higher Reynolds number, signifying an increase in the outer region contribution. Further, from figure 13(*d*), we observe that the width of this dominant source is around $0.25\delta$ since the *y*-coordinate is significant for $y < 0.25\delta$. Overall, at the low-frequency PSD peak, the contribution from the dominant mode peaks at $y^+ = 15$, and its width is around $0.25\delta$.

We create a representative net source field that gives the two-dimensional structure implied by a spectral POD mode. The representative field $\tilde{f}_G(x, y, z, t)$ implied by mode $\Phi_j(y, \omega_o)$ at frequency $\omega_o$ is constructed as

$$\tilde{f}_G(x, y, z, t) = Re(\alpha(x, z, \omega_o)\mathrm{e}^{-\mathrm{i}\angle\Phi_j(y,\omega_o)}|\Phi_j(y, \omega_o)|\mathrm{e}^{\mathrm{i}\omega_o t}), \tag{4.15}$$

where $Re(f)$ is the real part of $f$. Since $\alpha(x, z, \omega_o)$ is homogeneous in $x$ and $z$, we decompose it using the Fourier transform. Intuitively, we expect the streamwise convective Fourier component $\mathrm{e}^{-\mathrm{i}\omega_o x/c_o(\omega_o)}$ of $\alpha(x, z, \omega_o)$ to be the most dominant one. Here, $c_o(\omega_o)$ is the convective velocity at frequency $\omega_o$. For simplicity, we assume no spanwise variation of the representative net source. Substituting $\alpha(x, z, \omega_o) = \mathrm{e}^{-\mathrm{i}\omega_o x/c_o(\omega_o)}$ in the above equation, we obtain the representative field

$$\tilde{f}_G(x, y, z, t) = Re(\mathrm{e}^{-\mathrm{i}\omega_o x/c_o(\omega_o)}\mathrm{e}^{-\mathrm{i}\angle\Phi_j(y,\omega_o)}|\Phi_j(y, \omega_o)|\mathrm{e}^{\mathrm{i}\omega_o t}). \tag{4.16}$$

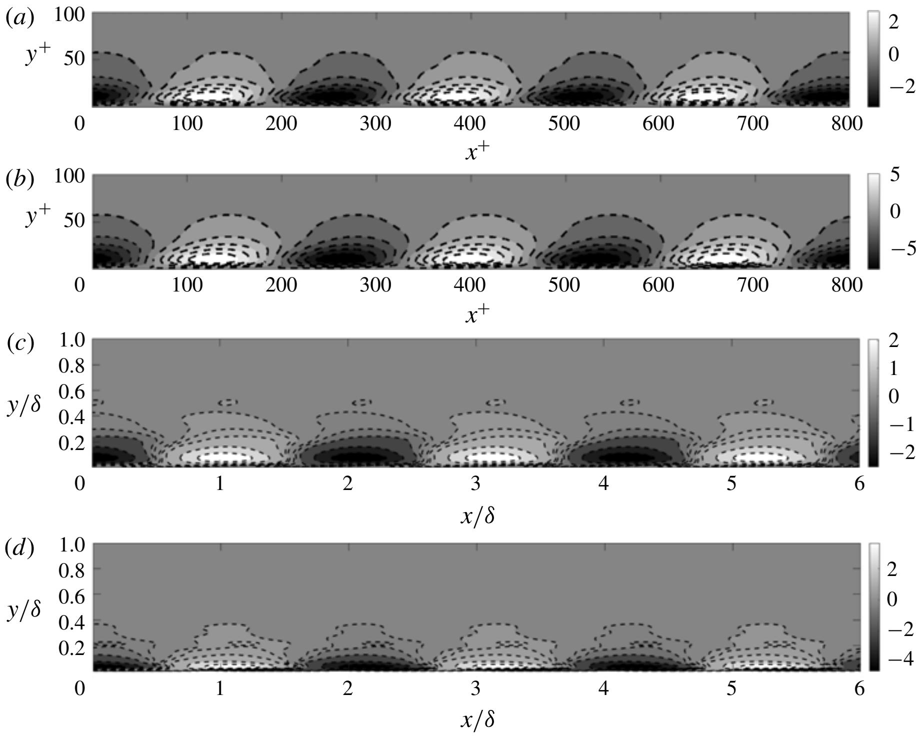


FIGURE 14. Representative net source $\tilde{f}_G$ at the premultiplied spectrum peak (*a*,*b*) and the linear spectrum peak (*c*,*d*). Panels (*a*,*c*) are for $Re_\tau = 180$, and (*b*,*d*) are for $Re_\tau = 400$. Contours in (*a*,*b*) are 10 equally spaced values between the minimum and maximum of $\tilde{f}_G$. Contours in (*c*,*d*) are [$\pm 0.05$ $\pm 0.1$ $\pm 0.2$ $\pm 0.5$ $\pm 0.8$] times the maximum value of $\tilde{f}_G$.

To create the representative field at a frequency $\omega_o$, we need three inputs – the mode $\Phi_j(y, \omega_o)$, the convection velocity $c_o(\omega_o)$ and the time $t$. Figure 14 shows the representative net source field constructed from the dominant spectral POD mode. Figures 14(*a*,*b*) are at the premultiplied PSD peak frequency and figures 14(*c*,*d*) are at the linear PSD peak frequency. We use a convection velocity defined as $c_o(\omega_o)/u_\tau = (\omega_o \delta/u_\tau)/k_p(\omega_o)\delta$, where $k_p(\omega_o)$ is the peak wavenumber coordinate at frequency $\omega_o$ in the wavenumber–frequency spectrum of wall-pressure. We choose time $t$ to be 0.

Figure 14(*a*,*b*) shows a convecting coherent structure inclined in the downstream direction. Essentially, this is because of the negative slope in the phase of the mode. As the inclined structures convect across a fixed streamwise location $x_o^+$, the wall-normal intensity (magnitude of the field that depends on $y$ and $x_o$) propagates towards the wall as indicated by the negative slope.

Figure 14(*c*,*d*) shows the coherent structure represented by the dominant POD mode at the linear PSD peak. These structures are vertical, with almost no inclination in the downstream direction, as indicated by almost no slope in the phase of the mode. Such large scale vertical patterns with streamwise spacing of $\sim 2\delta$ have been previously observed in the instantaneous rapid pressure fields for $Re_\tau \sim 1000$ by Abe *et al.* (2005). They proposed that these patterns are responsible for the low-wavenumber peak in the wall-pressure spectra. The coherent structures in figure 14(*c*,*d*) further support this case.

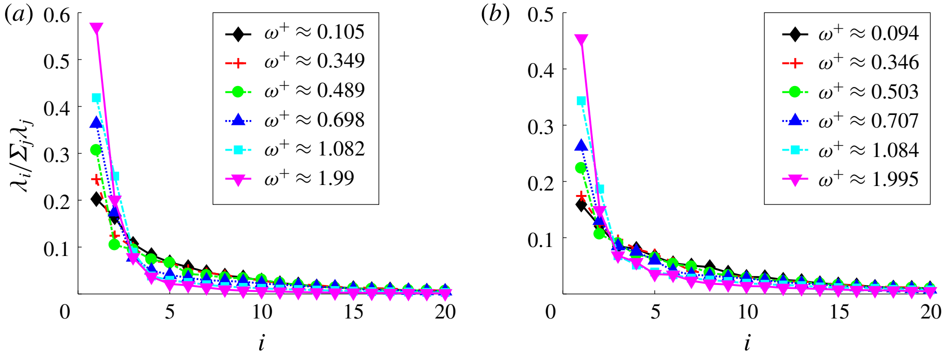


FIGURE 15. Spectral POD eigenvalues computed using the $L^2$ inner product for (*a*) $Re_\tau = 180$ and (*b*) $Re_\tau = 400$ at different frequencies.

Overall, the dominant spectral POD mode represents the active portion of the net source that contributes to the entire wall-pressure PSD. The remaining POD modes that comprise the inactive portion make zero contribution to the PSD. Further, the active and inactive parts are decorrelated. At high frequencies ($\omega^+ \geqslant 0.35$), the shape of the dominant POD mode is similar in inner units for the two $Re_\tau$. The two-dimensional (2-D) coherent structure at the premultiplied PSD peak inclines in the downstream direction. At the low-frequency linear PSD peak, the wall-normal contribution peaks in the buffer layer at $y^+ \approx 15$ with a width of $y/\delta \approx 0.25$. The corresponding 2-D structure has a large scale vertical pattern similar to the previous observations of the instantaneous rapid pressure field by Abe *et al.* (2005).

We expect the similarity of the high-frequency dominant modes in inner units to continue at even higher Reynolds numbers. In the low wavenumber/frequency wall-pressure linear spectrum peak, the outer region ($y^+ > 30$) contributes more for $Re_\tau =$ 400 than for $Re_\tau = 180$. This low wavenumber/frequency peak is present in the linear wall-pressure spectra up to $Re_\tau = 5000$ (Abe *et al.* 2005; Panton *et al.* 2017). With increasing Reynolds number, we expect this contribution from the outer region to grow larger. Further, at $Re_\tau \approx 5000$, the low- and high-wavenumber contributions to the premultiplied wall-pressure spectra show mild separation. We expect the spectral POD modes responsible for the low-wavenumber peak to depend on outer units. Further, high Reynolds number effects like amplitude modulation (Tsuji, Marusic & Johansson 2016) in the wall-pressure sources could be studied using the above spectral POD framework.

#### 4.3.1. *Remark on spectral POD with the $L^2$ inner product*

We also performed spectral POD of the net source CSD using the $L^2$ inner product. Figure 15 shows the obtained eigenvalues for both $Re_\tau$. The eigenvalues give the contribution of each POD mode to the wall-normal integral of the net source PSD. The POD modes obtained with the $L^2$ inner product, by definition, optimally decompose the integral of the net source PSD. However, the dominant POD mode might not contribute significantly to the wall-pressure PSD. Clearly, figure 16 shows this behaviour for $\omega^+ < 1$.

To investigate this further, we plot the index of the POD mode that contributes the most to the wall-pressure PSD as a function of frequency in figure 17. In the frequency ranges $0.55 < \omega^+ < 1$ and $\omega^+ > 1$, the dominant wall-pressure mode (largest $\gamma_i(\omega)$) is the second and the first spectral POD mode, respectively. At low frequencies

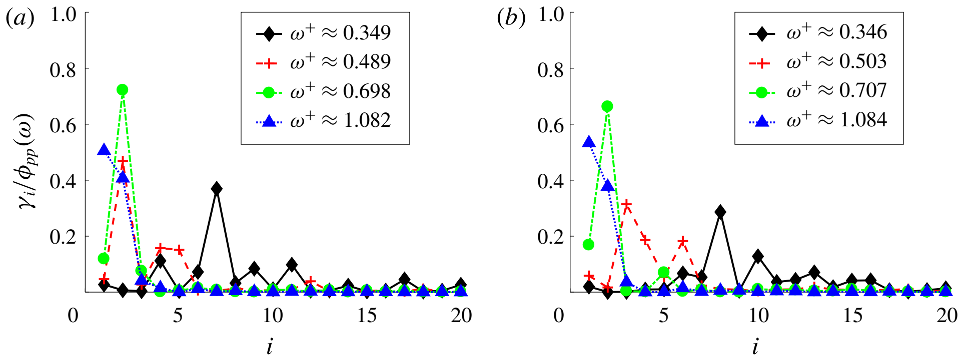


FIGURE 16. Contribution of the first 20 spectral POD modes computed using the $L^2$ inner product (normalized by the wall-pressure PSD) to wall-pressure PSD for (*a*) $Re_\tau = 180$ and (*b*) $Re_\tau = 400$ at different frequencies.

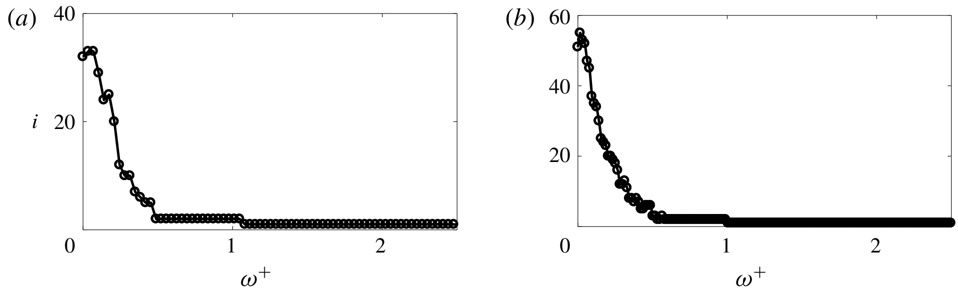


FIGURE 17. Index of the spectral POD (computed using $L^2$ inner product) that contributes the most to the wall-pressure PSD for (*a*) $Re_\tau = 180$ and (*b*) $Re_\tau = 400$.

$\omega^+ < 0.55$, the dominant wall-pressure mode index is larger than or equal to 3. The dominant spectral POD mode is not the dominant wall-pressure mode because of destructive interference. The contributions of the dominant spectral POD mode from different wall-normal regions cancel each other out. For more details, we refer the reader to appendix D.

The magnitude and phase of the first two dominant spectral POD modes at a high frequency of $\omega^+ \approx 1$ are shown in figure 18. Note that, for this frequency, the dominant spectral POD and wall-pressure modes coincide. Clearly, we observe that the dominant modes resemble wavepackets. For both $Re_\tau$, the envelope and phase of the wavepackets have a similar shape, which indicates similarity of the dominant modes at high frequencies. The envelope shows that dominant modes correspond to sources in the near-wall region ($y^+ < 30$). The first and second dominant mode envelopes have one and two lobes respectively (figure 18*a*,*c*). Since the slope of the phase variation of both modes is negative near the wall (figure 18*b*,*d*), equation (4.12) implies that these modes correspond to sources moving towards the wall.

Next, we investigate the first two dominant wall-pressure modes at $\omega^+ = 0.35$, which together contribute approximately 50 % to the wall-pressure PSD in figure 19. Note that the premultiplied spectrum peak occurs at this frequency (figure 1*b*). The magnitude and phase variation shows that these modes do not resemble a near-wall wavepacket. The envelope is not localized and the phase variation shows no sign of linear variation. Not much can be said of the pattern of these low-frequency

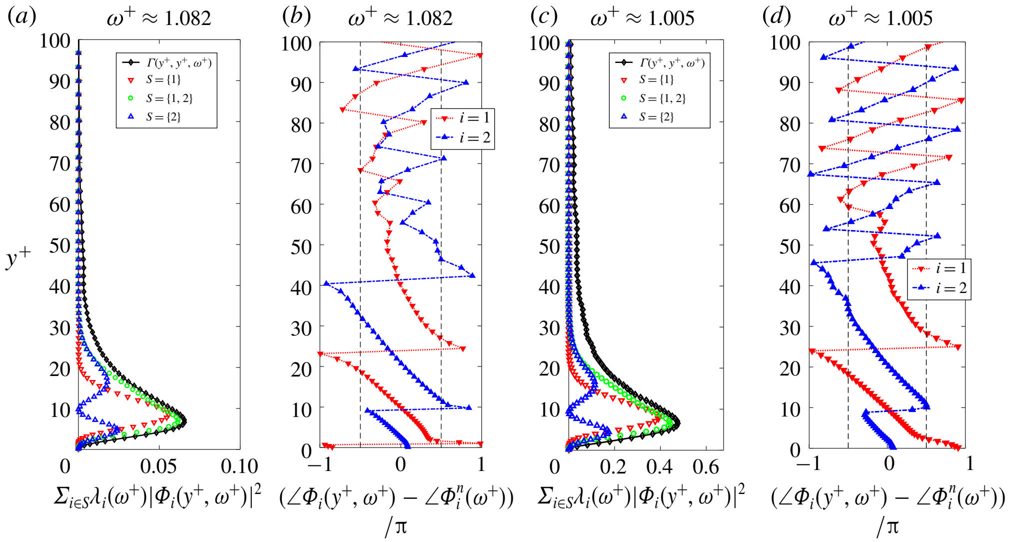

FIGURE 18. Envelope ($a$,$c$) and phase ($b$,$d$) of the two dominant spectral POD modes computed using the $L^2$ inner product at different frequencies. Panels ($a$,$b$) and ($c$,$d$) are for $Re_\tau = 180$ and 400, respectively. The left and right dashed black solid lines in ($b$,$d$) indicate $\angle\Phi_i(y^+, \omega^+) - \angle\Phi_i^n(\omega^+)$ equal to $-\pi/2$ and $\pi/2$, respectively.

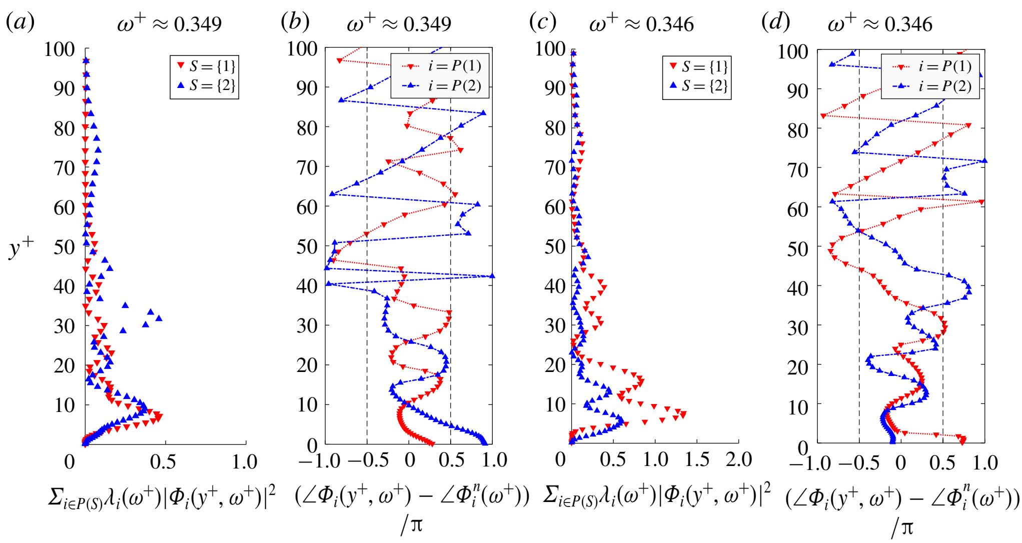

FIGURE 19. Envelope ($a$,$c$) and phase ($b$,$d$) of the two dominant wall-pressure modes computed using the $L^2$ inner product at $\omega^+ = 0.35$. Panels ($a$,$b$) and ($c$,$d$) are for $Re_\tau =$ 180 and 400, respectively. The left and right dashed black solid lines in ($b$,$d$) indicate $\angle\Phi_i(y^+, \omega^+) - \angle\Phi_i^n(\omega^+)$ equal to $-\pi/2$ and $\pi/2$, respectively. $P(S)$ is the spectral POD mode index of the $S$th dominant wall-pressure mode.

wall-pressure sources, except that the contributions from different wall-normal regions undergo constructive interference. This is because the phase of the mode varies mostly between the two dashed lines. Further, several suboptimal spectral POD modes each contribute a small fraction the wall-pressure PSD at this frequency (figure 16). Thus, the individual dominant wall-pressure mode obtained using the $L^2$ inner product does not give us much information of the wall-pressure sources. However, the mode obtained using the Poisson inner product with $\beta = 0.1$ (figure 12) gives useful information of the wall-pressure source.

Therefore, spectral POD using the Poisson inner product performs better than the $L^2$ inner product in isolating dominant wall-pressure sources for both low and high frequencies. This is because the Poisson inner product decomposes the integral $\iint_{-\delta}^{+\delta} (G(s, r, (\beta/1-\beta), 0)/1-\beta)\Gamma(r, s, \omega)\,\mathrm{d}r\,\mathrm{d}s$ as the sum of eigenvalues. For small enough $\beta$, this integral is a good proxy for wall-pressure PSD. On the other hand, the $L^2$ inner product decomposes the integrated net source PSD ($\int_{-\delta}^{+\delta} \Gamma(r, r, \omega), \mathrm{d}r$) instead which is not a good proxy for the wall-pressure PSD.

## 5. Summary

We present a novel framework to analyse the sources of wall-pressure fluctuation in turbulent channel flow. A net source function $f_G(y, t)$ is defined whose integral in the wall-normal direction gives the wall-pressure fluctuation, i.e. $p(t) = \int_{-\delta}^{+\delta} f_G(y, t)\,\mathrm{d}y$. The spectral properties of the defined net source function are studied by computing its CSD using the generated DNS dataset at $Re_\tau = 180$ and 400. The wall-pressure fluctuation – net source CSD shows a premultiplied peak at $\omega^+ = 0.35$ for both $Re_\tau$. The wall-normal location corresponding to the peak is $y^+ = 16.5$ and 18.4 for $Re_\tau =$ 180 and 400, respectively. Therefore, the peak in the premultiplied wall-pressure PSD at $\omega^+ = 0.35$ is due to the correlation with the sources in buffer layer. The wall-pressure fluctuation – net source CSD has a log-normal behaviour in $y^+$ for $\omega^+ >$ 0.35. The location of the dominant wall-parallel plane obtained from the mean of the log-normal profile varies exponentially with frequency. The wall-normal width of the dominant region obtained from the standard deviation of the log-normal profile is approximately proportional to the location of the dominant plane. At low frequencies, a dominant inner and overlap/outer region interaction is observed at both $Re_\tau$.

We obtain the decorrelated net source patterns by performing spectral POD of the net source CSD using an inner product that has a symmetric positive definite kernel. The net source can be decomposed into active and inactive parts. The dominant spectral POD mode identified with this new inner product is active in the sense that it contributes to the entire wall-pressure PSD. The remaining portion of the net source constituted by the suboptimal POD modes is inactive in the sense that it does not contribute to wall-pressure PSD. Further, the active and inactive portions of the net source are decorrelated.

The dominant mode at the premultiplied PSD peak ($\omega^+ \approx 0.35$) has a similar shape in inner units for both $Re_\tau$. It represents structures inclined in the downstream direction. At the low-frequency linear PSD peak, the wall-normal contribution peaks at $y^+ \approx 15$ and has a width of $y/\delta \approx 0.25$. The corresponding two-dimensional structure has a large scale vertical pattern similar to the observations of Abe *et al.* (2005) in the instantaneous fields of rapid pressure.

The analysis framework presented in this paper can be used to quantitatively understand the contribution of large scale coherent motions in the outer region to the wall-pressure PSD at very high Reynolds numbers. Such contributions are believed to be the reason for the increasing low wavenumber contribution to wall-pressure r.m.s. (Panton *et al.* 2017). The analysis has implications on wall-modelled large eddy simulations (LES). The wall-pressure fluctuation net source CSD shows that sources correlated with the buffer layer are essential contributors to the premultiplied power spectrum peak at $\omega^+ = 0.35$. However, in wall modelled LES where the first point is in the logarithmic layer, one would not resolve the net source terms that lie in the buffer region. Hence, wall-modelled LES would fail to accurately predict the wall-pressure spectra at high frequencies. These conclusions are consistent with Bradshaw (1967) who noted the importance of buffer layer eddies to the higher frequencies in the wall-pressure spectra, and are consistent with Park & Moin (2016) who attribute the errors in the high-frequency slope of wall-pressure spectrum to the lack of resolution of the buffer layer eddies in their wall-modelled LES. Also, high Reynolds number effects like amplitude modulation of the wall-pressure (Tsuji *et al.* 2016) can be studied using the above framework. The framework can also be used to quantitatively investigate the location of the sources that lead to $\omega^{-1}$ decay in the wall-pressure PSD at high Reynolds numbers.

## Acknowledgements

This work is supported by the United States Office of Naval Research (ONR) under grant N00014-17-1-2939 with Dr K.-H. Kim as the technical monitor. The computations were made possible through computing resources provided by the US Army Engineer Research and Development Center (ERDC) in Vicksburg, Mississippi on the Cray X6, Copper and Onyx of the High Performance Computing Modernization Program.

## Declaration of interests

The authors report no conflict of interest.

## Appendix A. Implementation details

The theory presented in § 3.1 considered infinite domains in the spanwise and streamwise directions. Here, we present the implementation for finite periodic domains instead. The integrals over the wavenumbers are replaced by a summation over the discrete wavenumbers that can be represented in the periodic domain. The wavenumber spacing is determined by the length of the domain in each direction.

Let $N_t$ be the number of time steps in each chunk used to compute the fast Fourier transform, $N_T$ be the total number of time steps for which the data are acquired, $n_c$ be the number of chunks used for temporal averaging the computed spectra, $T_c$ be the span of each chunk and $p_{ovp}$ be the percentage overlap between subsequent chunks.

The angular wavenumbers and frequencies are defined as

$$\left.\begin{gathered} k_l^x = \frac{2\pi l}{L_x}; \quad k_m^z = \frac{2\pi m}{L_z}; \quad \omega_n = \frac{2\pi n}{T_c}; \\ l = -N_x/2, \ldots, N_x/2 - 1; \quad m = -N_z/2, \ldots, N_z/2 - 1; \\ n = -N_t/2, \ldots, N_t/2 - 1. \end{gathered}\right\} \tag{A 1}$$

We store the source terms of the pressure Poisson equation in hard disk from the finite volume solver. The domain in the finite volume solver is split into multiple processors and each processor writes one file per run containing the time history of the source terms of the control volumes in its partition. A total of $\approx$ 8 TB and $\approx$ 30 TB was required to store the source terms of the pressure Poisson equation for the $Re_\tau = 180$ and $Re_\tau = 400$ cases respectively.

The portion of the time series that corresponds to the current chunk being processed is first converted to stationary frame of reference and then written to a scratch space as wall-parallel slices. Let $\bar{f}$ denote the four-dimensional source term array in the moving frame of reference corresponding to the current chunk. i.e.

$$\left.\begin{aligned}\bar{f}=\{\bar{f}_{i,j,k,l}\,|\,i=0,\ldots,N_x-1,j=0,\ldots,N_y-1,k=0,\ldots,N_z-1,\\ l=0,\ldots,N_t-1\},\\ \bar{f}_{i,j,k,l}=D_{x_n}u_mD_{x_m}u_n|_{x_i,y_j,z_k,t_l},\end{aligned}\right\} \tag{A 2}$$

where $D_{x_n}u_mD_{x_m}u_n$ is the discrete approximation to the right-hand side of the pressure Poisson equation. The data are converted to a stationary frame of reference using Fourier interpolation and stored in the source term array $f$ as

$$\left.\begin{aligned}f=\{f_{i,j,k,l}\,|\,i=1,\ldots,N_x,j=1,\ldots,N_y,k=1,\ldots,N_z,l=1,\ldots,N_t\},\\ f_{i,j,k,l}=\sum_{m=-N_x/2}^{N_x/2-1}\tilde{f}_{m,j,k,l}\mathrm{e}^{-\mathrm{i}k_m^xU_ct_l}\mathrm{e}^{\mathrm{i}k_m^xx_i},\\ \tilde{f}_{m,j,k,l}=\frac{1}{N_x}\sum_{i=0}^{N_x-1}\bar{f}_{i,j,k,l}\mathrm{e}^{-\mathrm{i}k_m^xx_i}.\end{aligned}\right\} \tag{A 3}$$

Multiple processors are used to transfer the data from the Cartesian decomposition of the solver to a wall-parallel decomposition of the computational domain. The wall-parallel decomposition facilitates the computation of the wavenumber frequency cross-spectra of the source terms. In order to obtain the fluctuation, the temporal mean of the array $f$ at each spatial point is subtracted to ensure that it has zero mean. i.e.

$$\left.\begin{aligned}f_{i,j,k,l}=f_{i,j,k,l}-\langle f\rangle_{i,j,k},\\ \langle f\rangle_{i,j,k}=\frac{1}{N_t}\sum_{l=0}^{N_t-1}f_{i,j,k,l}.\end{aligned}\right\} \tag{A 4}$$

Each of the wall-parallel slices stored in the scratch space is then Fourier transformed in streamwise, spanwise directions and in time. Let $\hat{f}$ denote the Fourier transformed $f$. Then,

$$\left.\begin{aligned}\hat{f}=\{\hat{f}_{i,j,k,l}\,|\,i=-N_x/2,\ldots,N_x/2-1,j=0,\ldots,N_y-1,\\ k=-N_z/2,\ldots,N_z/2-1,l=-N_t/2,\ldots,N_t/2-1\},\\ \hat{f}_{i,j,k,l}=\frac{1}{N_xN_zN_t}\sum_{m,n,p=1}^{N_x-1,N_z-1,N_t-1}f_{m,j,n,p}w_p\mathrm{e}^{-\mathrm{i}(k_i^xx_m+k_k^zz_n+\omega_lt_p)},\end{aligned}\right\} \tag{A 5}$$

where $w_p=\sin^2(\pi p/N_t)$ is the Hanning window function multiplied with the time series in order to avoid spectral leakage. The wall-parallel slice data are over written by its three-dimensional Fourier transform. The processors are split in the wall-normal and time directions to carry out the task in parallel and we use the parallel-FFTW (Frigo & Johnson 2005) library to carry out the Fourier transform.

As discussed in the previous section, the memory requirement to store the five-dimensional function $\phi_{ff}(r,s,k_1,k_3,\omega)$ is too large. We store and append the net source cross-spectral density sum array $\Gamma^s$ (defined below) instead. The possible $\{r_i, s_j\}_{i,j=1}^{N_y}$ pairs are split among multiple processors. For each $(r_i, s_j)$ pair, we read the arrays $\hat{f}_{:,i,:,:}$ and $\hat{f}_{:,j,:,:}$ from the scratch space and update the sum $\Gamma^s_{i,j,:}$ as

$$\left.\begin{aligned}
\Gamma^s &= \{\Gamma^s_{i,j,k} \mid i=1,\ldots,N_y, j=1,\ldots,N_y, k=-N_t/2,\ldots,N_t/2-1\},\\
\Gamma^s_{i,j,k} &= \Gamma^s_{i,j,k} + \frac{8}{3}\frac{T}{2\pi}\frac{L_1}{2\pi}\frac{L_3}{2\pi}\sum_{l=-N_x/2}^{N_x/2-1}\sum_{m=-N_z/2}^{N_z/2-1}\hat{f}^*_{l,i,m,k}\hat{f}_{l,j,m,k}G^*_{i,l,m}G_{j,l,m}\frac{2\pi}{L_1}\frac{2\pi}{L_3},\\
G_{i,l,m} &= G(0, y_i, k_l, k_m).
\end{aligned}\right\} \tag{A 6}$$

The factor 8/3 in the above equation accounts for the reduction in the spectral magnitude due to windowing (Bendat & Piersol 2011). The update to $\Gamma^s_{i,j,:}$ given in the above equation (A 6) is carried out in chunks along the frequency dimension due to limited memory available in a cluster node. The net source cross-spectral density $\Gamma$ array is then defined by dividing the $\Gamma^s$ array by the number of chunks $n_c$, i.e.

$$\Gamma = \{\Gamma_{i,j,k} \mid \Gamma_{i,j,k} = \Gamma^s_{i,j,k}/n_c, i=1,\ldots,N_y, j=1,\ldots,N_y, k=-N_t/2,\ldots,N_t/2-1\}. \tag{A 7}$$

We store and append only half of the entire $\Gamma^s$ array since $\Gamma_{j,i,k} = \Gamma^*_{i,j,k}$. We use 50 % overlap between the chunks to increase statistical convergence. As new chunk data become available, the net source cross-spectral density $\Gamma^s$ is updated.

Note that the Green's function had to be evaluated in quadruple precision for $Re_\tau = 400$ because for some wavenumbers, both the numerator and denominator were so large that it could not be stored in double precision. However, when divided, the resulting number could be stored in double precision. The above post-processing methodology is parallel, aware of the limited memory available in a supercomputer cluster node and can be used to analyse even larger channel flow datasets obtained for higher friction Reynolds numbers.

To obtain the spectral POD modes, we first obtain the eigenvalues $\{\lambda_{i,l}\}_{i=1}^{N_y}$ and the eigenvectors $\{\bar{\varphi}_{i,l}\}_{i=1}^{N_y}$ of the problem

$$\left.\begin{aligned}
A_l\bar{\varphi}_{i,l} &= \lambda_{i,l}W\bar{\varphi}_{i,l};\ i=1,\ldots,N_y,\ l=-N_t/2,\ldots,N_t/2-1,\\
A_l &= \{A_l \in \mathbb{C}^{N_y\times N_y} \mid \{A_l\}_{m,n} = \Delta y_m \Gamma_{m,n,l}\Delta y_n\},
\end{aligned}\right\} \tag{A 8}$$

where the matrix $W$ is the finite volume discretization of the operator $(-(1-\alpha)(\partial^2/\partial y^2) + \alpha)$. The spectral POD eigenvalues are $\{\lambda_{i,l}\}_{i=1}^{N_y}$ and eigenvectors are $\{\varphi_{i,l}\}_{i=1}^{N_y}$, where $\{\varphi_{i,l}\}_{i=1}^{N_y}$ is related to $\{\bar{\varphi}_{i,l}\}_{i=1}^{N_y}$ as

$$\left.\begin{aligned}
\varphi_{i,l} &= D^{-1}W\bar{\varphi}_{i,l};\ i=1,\ldots,N_y,\ l=-N_t/2,\ldots,N_t/2-1,\\
D &= \{D \in \mathbb{C}^{N_y\times N_y} \mid \{D\}_{m,n} = \Delta y_m\delta_{mn}\}.
\end{aligned}\right\} \tag{A 9}$$

## Appendix B. Orthogonality of the linear transformation $C$

We prove the orthogonality relation given by (3.22). Writing the Fourier transform of the net source function as a linear combination of the set of modes $\{\hat{\Phi}_i(y,\omega)\}_{i=1}^{\infty}$ and $\{\tilde{\Phi}_i(y,\omega)\}_{i=1}^{\infty}$, we have,

$$\hat{f}_G(x,y,z,\omega) = \sum_j \hat{\alpha}_j(x,z,\omega)\hat{\Phi}^*_j(y,\omega) = \sum_j \tilde{\alpha}_j(x,z,\omega)\tilde{\Phi}^*_j(y,\omega), \tag{B 1}$$

where $\hat{\alpha}(\omega)$ and $\tilde{\alpha}(\omega_o)$ are the coefficients of the linear combination. For brevity, we drop the dependence of $\hat{\alpha}$ and $\tilde{\alpha}$ on $x$ and $z$. Using (3.21) in (B 1) and equating the

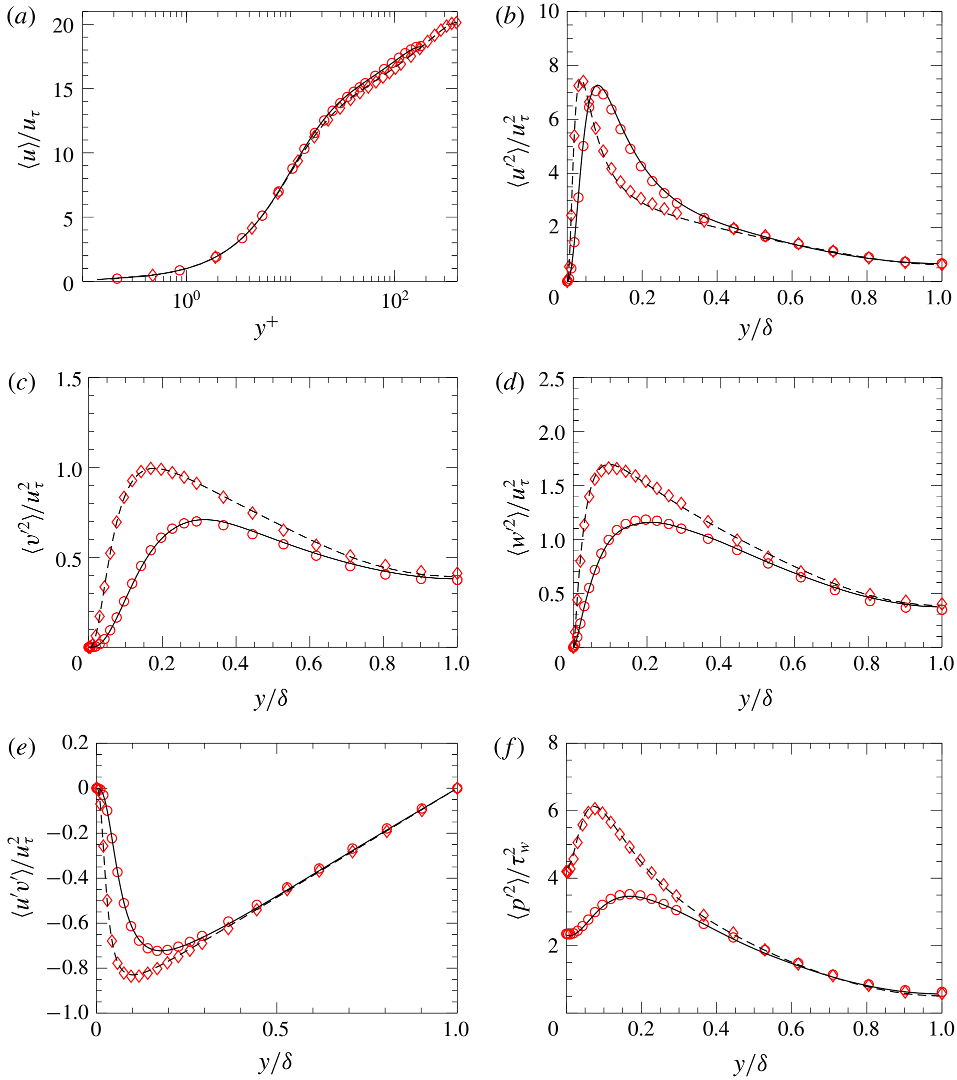


FIGURE 20. Velocity field and pressure fluctuation statistics. Solid and dashed lines denote the current DNS result at $Re_\tau = 180$ and 400, respectively. Circle and diamond symbols denote DNS data at $Re_\tau = 182$ and 392 from Moser, Kim & Mansour (1999). Panel (*a*) compares mean streamwise velocity, (*b*,*c*,*d*) compare mean-squared streamwise, wall-normal and spanwise velocity fluctuations, respectively, and (*e*,*f*) compare mean tangential Reynolds stress and mean-squared pressure fluctuation, respectively.

coefficients of $\{\tilde{\Phi}_j^*\}_{j=1}^{\infty}$, we have

$$\sum_j \hat{\alpha}_j(\omega) C_{jk}(\omega) = \tilde{\alpha}_k(\omega). \tag{B 2}$$

Correlating the coefficients, we have

$$\langle \tilde{\alpha}_k(\omega) \tilde{\alpha}_l^*(\omega_o) \rangle = \sum_j \sum_m \langle \hat{\alpha}_j(\omega) \hat{\alpha}_m(\omega_o) \rangle C_{jk}(\omega) C_{ml}^*(\omega_o). \tag{B 3}$$

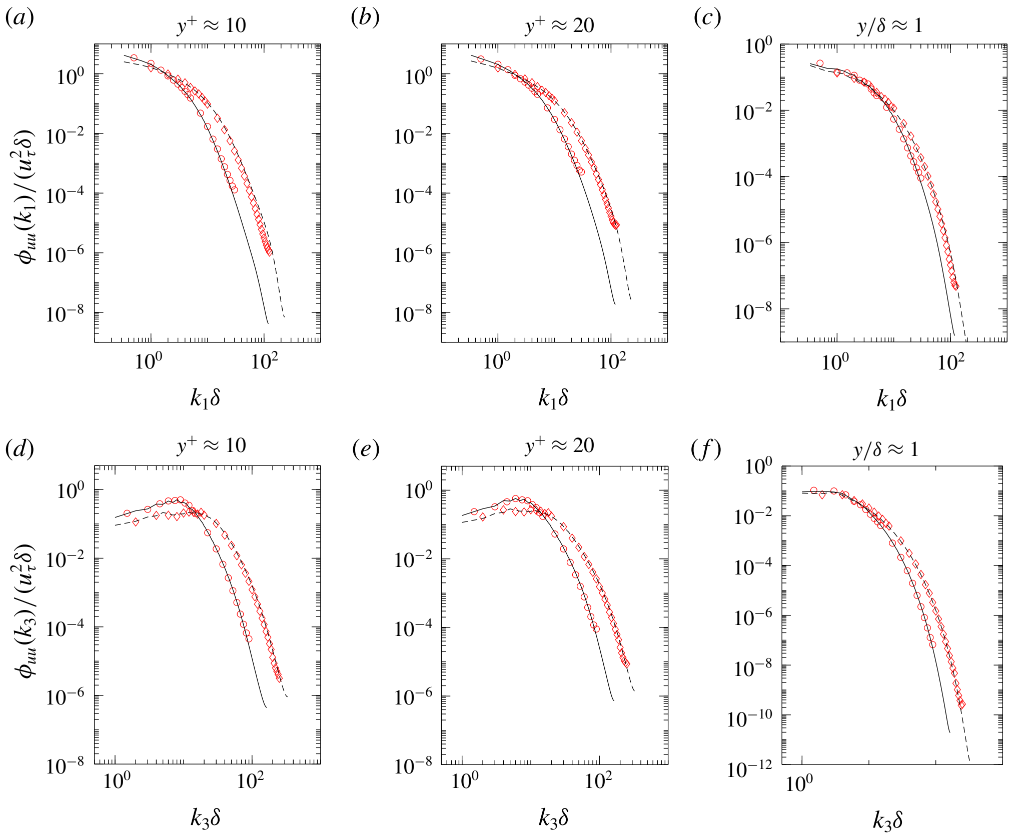


FIGURE 21. Streamwise velocity fluctuation spectra. Panels (*a–c*) and (*d–f*) are streamwise and spanwise wavenumber spectra, respectively, at different wall-normal locations. Solid and dashed lines denote the current DNS result at $Re_\tau = 180$ and 400, respectively. Circle and diamond symbols denote DNS data at $Re_\tau = 182$ and 392 from Moser *et al.* (1999).

Since the coefficients are decorrelated, we obtain

$$\tilde{\lambda}_k(\omega)\delta_{kl}\delta(\omega-\omega_o) = \sum_j \sum_m \hat{\lambda}_j \delta_{jm}\delta(\omega-\omega_o) C_{jk}(\omega) C^*_{ml}(\omega_o). \tag{B 4}$$

Integrating in $\omega_o$ and expression the above relation in matrix form, we have

$$\tilde{\Lambda}(\omega) = C^H(\omega)\hat{\Lambda}(\omega)C(\omega), \tag{B 5}$$

where $\tilde{\Lambda}(\omega)$ and $\hat{\Lambda}(\omega)$ are the diagonal matrices of the eigenvalues. Since the eigenvalues are non-negative, we decompose $\hat{\Lambda}(\omega)$ as $\hat{\Lambda}^{1/2}(\omega)\hat{\Lambda}^{1/2}(\omega)$, respectively, where $\Lambda^{1/2}(\omega)$ is a diagonal matrix constructed using the set of values $\{\sqrt{\lambda_i(\omega)}\}_{i=1}^{\infty}$, and obtain the required result

$$(\hat{\Lambda}^{1/2}(\omega)C(\omega))^H \hat{\Lambda}^{1/2}(\omega)C(\omega) = \tilde{\Lambda}(\omega). \tag{B 6}$$

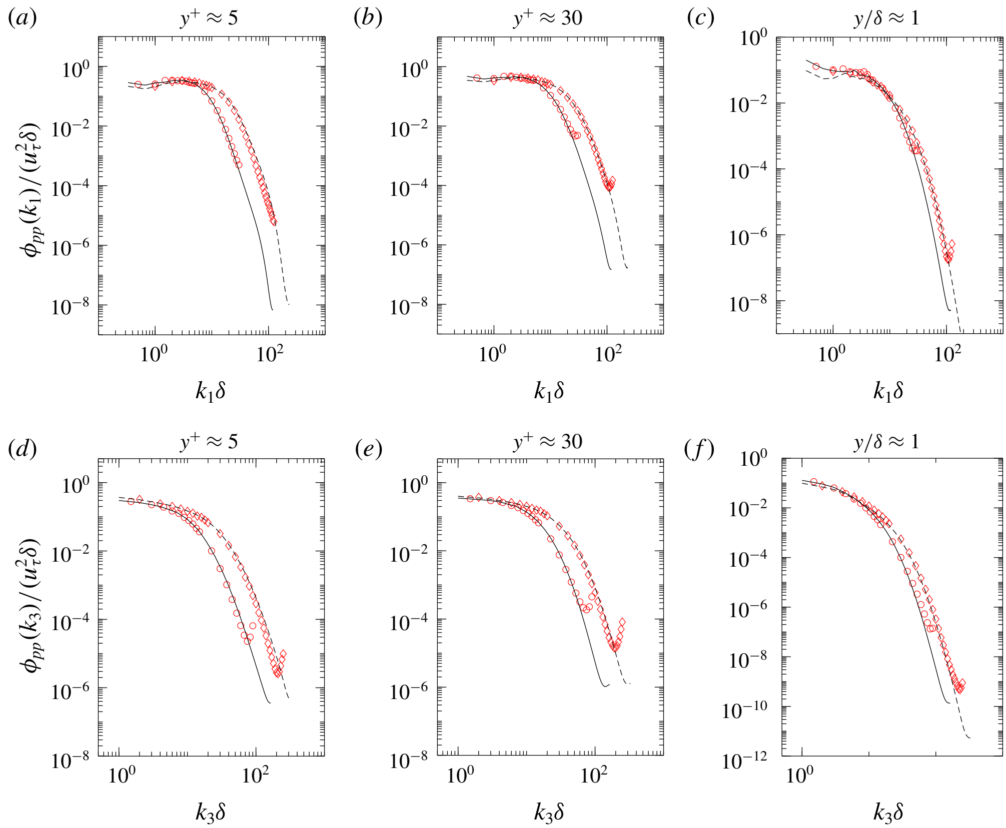


FIGURE 22. Pressure fluctuation spectra. Panels (*a–c*) and (*d–f*) are streamwise and spanwise wavenumber spectra, respectively, at different wall-normal locations. Solid and dashed lines denote the current DNS result at $Re_\tau = 180$ and 400, respectively. Circle and diamond symbols denote DNS data at $Re_\tau = 182$ and 392 from Moser *et al.* (1999).

## Appendix C. DNS validation

We compare the mean, intensities and spectra from the current DNS to the previous reference DNS. We sample the velocity and pressure field every 50 time steps to compute the statistics presented in this section.

Figure 20 shows the comparison of velocity field and pressure fluctuation statistics to the previous DNS of Moser *et al.* (1999) performed at $Re_\tau = 182$ and 392. Figure 20(*a*) compares mean streamwise velocity. Figures 20(*b*), 20(*c*) and 20(*d*) compare mean-squared streamwise, wall-normal and spanwise velocity fluctuations, respectively. Figures 20(*e*) and 20(*f*) compare mean tangential Reynolds stress and mean-squared pressure fluctuation, respectively. We observe good agreement in the compared quantities.

Figure 21 compares both streamwise and spanwise wavenumber spectra of the streamwise velocity fluctuations to the previous DNS of Moser *et al.* (1999) at different wall-normal locations. We compare the spectra at $y^+ \approx 10$ (near the buffer layer peak in the intensity), $y^+ \approx 20$ and $y/\delta \approx 1$ (channel centreline). The current spectra agree well both near the wall and at the channel centre for the two $Re_\tau$. Therefore, the DNS is well resolved.

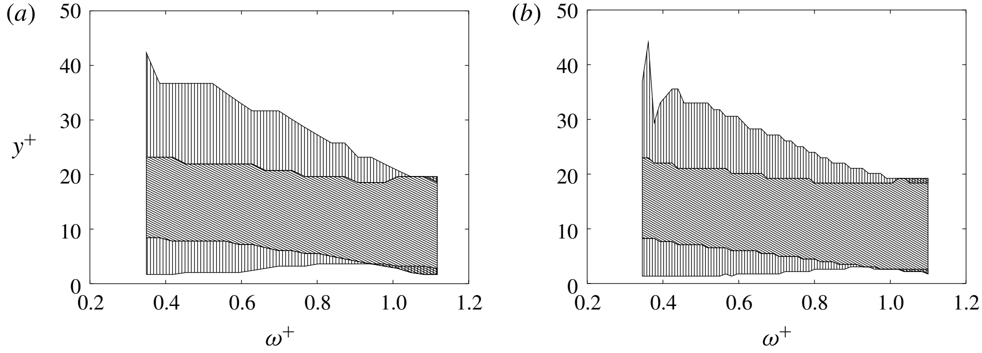


FIGURE 23. Comparison of destructively interfering regions of the dominant spectral POD mode computed using the $L^2$ inner product as a function of frequency for (*a*) $Re_\tau = 180$ and (*b*) $Re_\tau = 400$. In the cross and vertically hatched regions, $|\angle\Phi_i(y^+, \omega^+) - \angle\Phi_i^n(\omega^+)| < \pi/2$ and $\pi/2 < |\angle\Phi_i(y^+, \omega^+) - \angle\Phi_i^n(\omega^+)| < \pi$, respectively.

In figure 22, we compare the streamwise and spanwise wavenumber spectra of the pressure fluctuations to Moser *et al.* (1999) at $y^+ \approx 5$ (near the wall), $y^+ \approx 30$ (at the peak intensity location) and $y/\delta \approx 1$ (channel centreline). The spectra show good agreement. Also, we do not observe the spurious pile up of the spectrum levels at very high wavenumbers seen in the results of Moser *et al.* (1999).

## Appendix D. Destructive interference of dominant $L^2$ inner product mode contribution to wall-pressure PSD

We investigate the frequency dependence of the destructive interference of the obtained dominant spectral POD mode (computed using the $L^2$ inner product) in figure 23. The envelope and the phase of the wavepacket are used to identify destructively interfering regions. In the figure, the vertical and cross-hatched regions of the mode interfere destructively. In the cross-hatched and vertically hatched regions, the phase satisfies $|\angle\Phi_i(y, \omega) - \angle\Phi_i^n(\omega)| < \pi/2$ and $\pi/2 < |\angle\Phi_i(y, \omega) - \angle\Phi_i^n(\omega)| < \pi$, respectively. With increase in frequency, the ratio of the cross and vertically hatched region increases. Therefore, the destructive interference in the contribution from the dominant spectral POD mode to wall-pressure PSD decreases. Hence, the dominant spectral POD mode becomes the dominant wall-pressure mode for $\omega^+ \geqslant 1$ (figure 17). For small frequencies, the dominant spectral POD mode does not resemble a wall-normal wavepacket. Hence, we would not obtain a continuously (continuous in frequency) varying interface between the destructively interfering region. Therefore, we do not include the frequencies below $\omega^+ = 0.35$.

## REFERENCES

ABE, H., MATSUO, Y. & KAWAMURA, H. 2005 A DNS study of Reynolds-number dependence on pressure fluctuations in a turbulent channel flow. In *Fourth International Symposium on Turbulence and Shear Flow Phenomena*. Begel House Inc.

BENDAT, J. S. & PIERSOL, A. G. 2011 *Random Data: Analysis and Measurement Procedures*. John Wiley & Sons.

BERNARDINI, M., PIROZZOLI, S., QUADRIO, M. & ORLANDI, P. 2013 Turbulent channel flow simulations in convecting reference frames. *J. Comput. Phys.* **232**, 1–6.

BLAKE, W. K. 1970 Turbulent boundary-layer wall-pressure fluctuations on smooth and rough walls. *J. Fluid Mech.* **44**, 637–660.

BLAKE, W. K. 2017 *Mechanics of Flow-Induced Sound and Vibration,* vols 1 and 2. Academic.

BRADSHAW, P. 1967 Inactive-motion and pressure fluctuations in turbulent boundary layers. *J. Fluid Mech.* **30** (2), 241–258.

BULL, M. K. 1996 Wall-pressure fluctuations beneath turbulent boundary layers: some reflections on forty years of research. *J. Sound Vib.* **190**, 299–315.

CHANG, P. A. III, PIOMELLI, U. & BLAKE, W. K. 1999 Relationship between wall pressure and velocity-field sources. *Phys. Fluids* **11**, 3434–3448.

CHOI, H. & MOIN, P. 1990 On the space–time characteristics of wall-pressure fluctuations. *Phys. Fluids* **2**, 1450–1460.

CORCOS, G. M. 1964 The structure of the turbulent pressure field in boundary-layer flows. *J. Fluid Mech.* **18**, 353–378.

DE GRAAFF, D. B. & EATON, J. K. 2000 Reynolds-number scaling of the flat-plate turbulent boundary layer. *J. Fluid Mech.* **422**, 319–346.

DEL ÁLAMO, J. C. & JIMÉNEZ, J. 2003 Spectra of the very large anisotropic scales in turbulent channels. *Phys. Fluids* **15**, L41–L44.

FARABEE, T. M. & CASARELLA, M. J. 1991 Spectral features of wall pressure fluctuations beneath turbulent boundary layers. *Phys. Fluids* **3**, 2410–2420.

FRIGO, M. & JOHNSON, S. G. 2005 The design and implementation of FFTW3. *Proc. IEEE* **93**, 216–231.

GEROLYMOS, G. A., SÉNÉCHAL, D. & VALLET, I. 2013 Wall effects on pressure fluctuations in turbulent channel flow. *J. Fluid Mech.* **720**, 15–65.

GRAVANTE, S. P., NAGUIB, A. M., WARK, C. E. & NAGIB, H. M. 1998 Characterization of the pressure fluctuations under a fully developed turbulent boundary layer. *AIAA J.* **36**, 1808–1816.

HOYAS, S. & JIMÉNEZ, J. 2006 Scaling of the velocity fluctuations in turbulent channels up to Re $\tau = 2003$. *Phys. Fluids* **18** (1), 011702.

HU, Z., MORFEY, C. L. & SANDHAM, N. D. 2006 Wall pressure and shear stress spectra from direct numerical simulations of channel flow. *AIAA J.* **44**, 1541–1549.

HUANG, N. E. & SHEN, S. P. 2014 *Hilbert–Huang Transform and its Applications*. World Scientific.

JIMENEZ, J. & HOYAS, S. 2008 Turbulent fluctuations above the buffer layer of wall-bounded flows. *J. Fluid Mech.* **611**, 215–236.

KIM, J. 1989 On the structure of pressure fluctuations in simulated turbulent channel flow. *J. Fluid Mech.* **205**, 421–451.

KIM, J. & HUSSAIN, F. 1993 Propagation velocity of perturbations in turbulent channel flow. *Phys. Fluids* A **5** (3), 695–706.

KIM, J., MOIN, P. & MOSER, R. 1987 Turbulence statistics in fully developed channel flow at low Reynolds number. *J. Fluid Mech.* **177**, 133–166.

KLEWICKI, J. C., PRIYADARSHANA, P. J. A. & METZGER, M. M. 2008 Statistical structure of the fluctuating wall pressure and its in-plane gradients at high Reynolds number. *J. Fluid Mech.* **609**, 195–220.

LUMLEY, J. L. 2007 *Stochastic Tools in Turbulence*. Courier Corporation.

MAHESH, K., CONSTANTINESCU, G. & MOIN, P. 2004 A numerical method for large-eddy simulation in complex geometries. *J. Comput. Phys.* **197**, 215–240.

MORRISON, J. F. 2007 The interaction between inner and outer regions of turbulent wall-bounded flow. *Phil. Trans. R. Soc. Lond.* A **365**, 683–698.

MOSER, R. D., KIM, J. & MANSOUR, N. N. 1999 Direct numerical simulation of turbulent channel flow up to $Re_\tau = 590$. *Phys. Fluids* **11** (4), 943–945.

PANTON, R. L., LEE, M. & MOSER, R. D. 2017 Correlation of pressure fluctuations in turbulent wall layers. *Phys. Rev. Fluids* **2**, 094604.

PARK, G. I. & MOIN, P. 2016 Space–time characteristics of wall-pressure and wall shear-stress fluctuations in wall-modeled large eddy simulation. *Phys. Rev. Fluids* **1**, 024404.

POPE, S. B. 2001 *Turbulent Flows*. Cambridge University Press.

SCHMIDT, O. T., TOWNE, A., RIGAS, G., COLONIUS, T. & BRÈS, G. A. 2018 Spectral analysis of jet turbulence. *J. Fluid Mech.* **855**, 953–982.

SILLERO, J. A., JIMÉNEZ, J. & MOSER, R. D. 2013 One-point statistics for turbulent wall-bounded flows at Reynolds numbers up to $\delta^+ \approx 2000$. *Phys. Fluids* **25**, 105102.

TOWNE, A., SCHMIDT, O. T. & COLONIUS, T. 2018 Spectral proper orthogonal decomposition and its relationship to dynamic mode decomposition and resolvent analysis. *J. Fluid Mech.* **847**, 821–867.

TSUJI, Y., FRANSSON, J. H. M., ALFREDSSON, P. H. & JOHANSSON, A. V. 2007 Pressure statistics and their scaling in high-Reynolds-number turbulent boundary layers. *J. Fluid Mech.* **585**, 1–40.

TSUJI, Y., MARUSIC, I. & JOHANSSON, A. V. 2016 Amplitude modulation of pressure in turbulent boundary layer. *Intl J. Heat Fluid Flow* **61**, 2–11.

WILLMARTH, W. W. 1975 Pressure fluctuations beneath turbulent boundary layers. *Annu. Rev. Fluid Mech.* **7**, 13–36.

WILLMARTH, W. W. & WOOLDRIDGE, C. E. 1962 Measurements of the fluctuating pressure at the wall beneath a thick turbulent boundary layer. *J. Fluid Mech.* **14**, 187–210.